JOURNAL OF THE MECHANICAL BEHAVIOR OF BIOMEDICAL MATERIALS 62 (2016) 515–533

Available online at www.sciencedirect.com

ScienceDirect

www.elsevier.com/locate/jmbbm

Research Paper

Anisotropic constitutive model incorporating multiple damage mechanisms for multiscale simulation of dental enamel

Songyun Ma[a,*], Ingo Scheider[a], Swantje Bargmann[a,b]

[a]Institute of Materials Research, Materials Mechanics/ACE-Centre, Helmholtz-Zentrum Geesthacht, Germany
[b]Institute of Continuum Mechanics and Material Mechanics, Hamburg University of Technology, Germany

ARTICLE INFO

Article history:
Received 29 March 2016
Received in revised form
23 May 2016
Accepted 24 May 2016
Available online 3 June 2016

Keywords:
Anisotropic hyperelastic damage model
Dental enamel
Bio-composite
Numerical homogenization
3D micromechanical simulation
Multiple damage mechanisms

ABSTRACT

An anisotropic constitutive model is proposed in the framework of finite deformation to capture several damage mechanisms occurring in the microstructure of dental enamel, a hierarchical bio-composite. It provides the basis for a homogenization approach for an efficient multiscale (in this case: multiple hierarchy levels) investigation of the deformation and damage behavior. The influence of tension–compression asymmetry and fiber–matrix interaction on the nonlinear deformation behavior of dental enamel is studied by 3D micromechanical simulations under different loading conditions and fiber lengths. The complex deformation behavior and the characteristics and interaction of three damage mechanisms in the damage process of enamel are well captured. The proposed constitutive model incorporating anisotropic damage is applied to the first hierarchical level of dental enamel and validated by experimental results. The effect of the fiber orientation on the damage behavior and compressive strength is studied by comparing micro-pillar experiments of dental enamel at the first hierarchical level in multiple directions of fiber orientation. A very good agreement between computational and experimental results is found for the damage evolution process of dental enamel.

1. Introduction

Dental enamel exhibits both high strength and high toughness simultaneously in spite of a high volume fraction of fibrous hydroxyapatite (90%), a mineral with generally brittle fracture behavior (Fratzl and Weinkamer, 2007). Many studies on the structure–property relationship reveal that nano-sized mineral fibers aligned in a staggered manner in the hierarchical microstructure lead to extraordinary mechanical properties (Chen et al., 2012; Bechtle et al., 2012). Recently, many groups mimic the building principle of dental enamel for developing bio-inspired nano-composites for high performance components (Chen and Pugno, 2013; Espinosa et al., 2009; Humburg et al., 2014). For this purpose, micromechanical models have been proposed and developed to

*Corresponding author.
E-mail address: songyun.ma@hzg.de (S. Ma).

http://dx.doi.org/10.1016/j.jmbbm.2016.05.033

clarify the relationship between the unique microstructure and the high damage resistance of enamel (An et al., 2015; Scheider et al., 2015).

Due to the anisotropy of the microstructure and complex damage mechanisms, the deformation and damage modeling of dental enamel are still challenging tasks. Most research efforts focus on modeling the deformation and damage behavior under uniaxial tensile loading perpendicular to the fiber direction (Jäger and Fratzl, 2000; Gao et al., 2003; Bar-On and Wagner, 2011). However, enamel is mainly loaded by compressive and shear forces during mastication and chewing cycles (Yilmaz et al., 2015). Furthermore, the orientation of mineral fibers strongly depends on the location in the enamel and the hierarchical level. Therefore, the investigation of the deformation and damage behavior under compressive loading in fiber direction and inclined to the fiber is crucial for understanding the structure–property relationship of enamel. In addition, linking microstructural characteristics to the macroscopic behavior is necessary for simulating the (homogenized) mechanical response of enamel at higher hierarchical levels and estimating the critical loading of components made by bio-inspired nano-composites. To this end, in the present work, an anisotropic damage model is developed in the framework of continuum damage mechanics and validated by a 3D micro-mechanical model under different tensile, compressive loadings.

In recent years, extensive experimental and computational studies at different length-scales contributed to describe the correlation between high damage tolerance and micro-structural features of enamel, e.g., the aspect ratio of mineral fiber, the fraction of protein, the arrangement of the mineral fiber, as well as the hierarchical structure (Bargmann et al., 2013; An et al., 2012; Bechtle et al., 2010). Barthelat (2014) elaborated a step-by-step approach to design and optimize staggered composites by employing a periodic micro-mechanical model including a failure criterion for the mineral fiber based on fracture mechanics. Lu et al. (2012) introduced a monoclinic anisotropic model based on a 3D micromechanical analysis, which takes into account the orientation changes of the hydroxyapatite crystals and their spatial elastic property variations. An et al. (2012) performed multiscale numerical simulations and found that the non-uniform arrangement of mineral crystallites in prisms enhances the energy dissipation and retains sufficient stiffness for the outer enamel. The majority of these models focused on modeling tensile behavior of enamel based on the small deformation theory. Very limited effort was dedicated to investigate the influence of the mineral fiber orientation on the damage behavior and strength of enamel in the framework of finite deformation. However, this is important for developing a general 3D constitutive model of enamel and must be taken into account to accurately predict the damage accumulation process at different hierarchical levels.

Since dental enamel can be regarded as a fiber reinforced bio-composite with a hierarchical structure, constitutive models for nonlinear anisotropic deformation behavior of fiber reinforced materials in the finite deformation regime can be applied. In the past decades, a large number of phenomenological hyperelastic models have been proposed (Ogden, 1972; Yeoh, 1993; Ehret and Itskov, 2009) for modeling the deformation and damage behavior of bio-composites. deBotton et al. (2006) proposed a transversely isotropic hyperelastic model accounting for material response under out-of-plane and in-plane shear loading modes. Peng et al. (2006) introduced a new term accounting for the fiber–matrix interaction into the strain energy density function. Gasser et al. (2006) developed a hyperelastic potential depending on direction dependent invariants for transversely isotropic material, in particular soft biological tissues. Guo et al. (2014) demonstrated a numerical homogenization approach for predicting the overall mechanical response of the composite under different loading conditions.

In order to simulate the damage behavior of fiber-reinforced composites, continuum damage mechanics has widely been applied to describe the damage accumulation process in different damage modes (Chaboche et al., 1995; Lapczyk and Hurtado, 2007; Maimí et al., 2007; Peña, 2011; Mengoni and Ponthot, 2015; Vasiukov et al., 2015). However, there exists no model capturing the features of matrix damage, fiber damage and interface debonding simultaneously and their interactions with sufficient accuracy. In the present work, an anisotropic damage model is proposed in the framework of finite deformation mapping (i) debonding of interface between mineral fiber and protein, (ii) damage of matrix and (iii) breaking of mineral fibers. A hyperelastic model that describes the nonlinear deformation behavior under various loading condition builds the basis for a proper damage model. Particularly, the influence of tension–compression asymmetry and fiber–matrix interaction on the deformation behavior of dental enamel is studied in 3D micromechanical simulations.

The damage process incorporating different damage mechanisms is studied numerically for dental enamel as a role nano-composite with high and low fiber aspect ratios, which involve two typical failure mechanisms, i.e., the breaking of the fiber (for high aspect ratio) and degradation of interface and matrix (for low aspect ratio). The present model is applied to the first hierarchy level for investigating its predictive capability. Further, the simulation results are compared to experimental results from micro-cantilever beam and micro-pillar experiments. Finally, the effect of the fiber orientation on the damage behavior and compressive strength is investigated.

The novel homogenized damage model, which is developed based on RVE simulations, is able to predict the averaged behavior of the microstructure and take into account the different failure mechanisms by means of distinct damage variables as internal variables. The numerical homogenized approach presented in this work can be applied to higher hierarchical levels for efficiently studying structure–property relationship at higher hierarchical levels and the role of the hierarchical level on the damage-tolerance behavior, since dental enamel can be regarded as a bio-composite with a self-similar structure at each hierarchical level.

2. Anisotropic hyperelastic damage model of dental enamel

As outlined in the introduction, dental enamel possesses a fibrous microstructure with several hierarchy levels. In order to predict the mechanical response, a homogenized constitutive model based on the microstructure at a lower hierarchical level is required to capture the anisotropic response of the material at higher hierarchical levels. The anisotropy results from the presence of a unidirectional alignment of mineral fibers. In this section, an anisotropic damage model is developed to describe the homogenized deformation and damage behavior of dental enamel at the first hierarchical level. The model is formulated within the framework of finite deformation, since the macroscopic fracture strain can reach up to 10% in micro-pillar tests and the local deformation can be much larger due to the debonding of interface and localization of strains.

2.1. Kinematics of finite deformation

Following the standard concept for describing the deformation of material, $\boldsymbol{X}$ and $\boldsymbol{x}$ denote the position vectors of a material particle in the reference and current configurations, respectively. The direction vector of fibers in the reference configuration is denoted by $\mathbf{a}_0$. The deformation gradient $\mathbf{F}$ is defined as $\mathbf{F}=\frac{\partial \mathbf{x}}{\partial \mathbf{X}}$. The relevant strain invariants of the right Cauchy–Green deformation tensor $\mathbf{C}=\mathbf{F}^t\cdot\mathbf{F}$ used throughout the investigation are given as:

$$I_1=\operatorname{tr}\mathbf{C};\quad I_2=\tfrac{1}{2}\left[\operatorname{tr}^2\mathbf{C}-\operatorname{tr}\mathbf{C}^2\right];\quad I_3=\det\mathbf{C}=J^2;$$
$$I_4=\mathbf{a}_0\cdot\mathbf{C}\cdot\mathbf{a}_0;\quad I_5=\mathbf{a}_0\cdot\mathbf{C}^2\cdot\mathbf{a}_0; \tag{1}$$

A multiplicative decomposition of $\mathbf{F}$ into dilatation and isochoric parts is used here, since damage might act differently on these deformation modes (Flory, 1961; Gasser et al., 2006): $\overline{\mathbf{F}}=J^{-1/3}\mathbf{F}$, with $J=\det\mathbf{F}$. Correspondingly, the right isochoric Cauchy–Green deformation tensor is defined as $\overline{\mathbf{C}}=\overline{\mathbf{F}}^t\cdot\overline{\mathbf{F}}=J^{-2/3}\mathbf{C}$. Its first strain invariant reads $\overline{I}_1=\operatorname{tr}\overline{\mathbf{C}}$.

2.2. Damage model within the framework of thermodynamics at finite deformation

Based on the knowledge from the small scale testings and multiscale simulations, an anisotropic damage model is proposed to describe the damage process of dental enamel. Regarding the characteristics of deformation and damage behavior of dental enamel, the Helmholtz free energy density is divided into four parts:

$$\Psi=\Psi_{\mathrm{m}}(D_{\mathrm{m}},I_1,I_3)+\Psi_{\mathrm{f}}(D_{\mathrm{f}},D_{\mathrm{int}},I_4)+\Psi_{\mathrm{int}}(I_1,I_2,I_3,I_4,I_5,D_{\mathrm{int}})+\Psi_{\mathrm{D}}(\alpha), \tag{2}$$

where D_{m}, D_{f} and D_{int} are defined as matrix damage, fiber damage and interface damage, respectively. Ψ_{m} and Ψ_{f} are the corresponding free energy density terms of matrix and mineral fiber. Ψ_{int} is the free energy density induced by the fiber–matrix shear interaction. Ψ_{D} is the free energy density related to the internal variable of the damage strengthening in the matrix and the interface, α. Internal forces in fibers are transported by the interface from the matrix and contribute to the damage of the interface. Thus, the interface damage D_{int} occurs in the free energy terms of the fiber as well as the fiber–matrix interaction.

The constitutive model should be consistent with thermodynamic laws and principles of continuum mechanics. The material's damage process is an irreversible process obeying the second law of thermodynamics. This is exploited by means of the Clausius–Duhem inequality for the dissipation $\mathfrak{D}_{\mathrm{int}}$ as (Coleman and Noll, 1963)

$$\mathfrak{D}_{\mathrm{int}}=\tfrac{1}{2}\mathbf{S}:\dot{\mathbf{C}}-\dot{\Psi}\geq 0 \tag{3}$$

in the isothermal case, where $\mathbf{S}$ is the second Piola–Kirchhoff stress tensor. Inserting Eq. (2) into Eq. (3), the Clausius–Duhem inequality reads

$$\mathfrak{D}_{\mathrm{int}}=\left[\mathbf{S}-2\frac{\partial\Psi}{\partial\mathbf{C}}\right]:\frac{\dot{\mathbf{C}}}{2}-\frac{\partial\Psi}{\partial D_{\mathrm{m}}}\dot{D}_m-\frac{\partial\Psi}{\partial D_{\mathrm{f}}}\dot{D}_f-\frac{\partial\Psi}{\partial D_{\mathrm{int}}}\dot{D}_{\mathrm{int}}-\frac{\partial\Psi}{\partial\alpha}\dot{\alpha}\geq 0. \tag{4}$$

Consequently, the second Piola–Kirchhoff stress tensor must satisfy

$$\mathbf{S}=2\frac{\partial\Psi}{\partial\mathbf{C}}, \tag{5}$$

since the Clausius–Duhem inequality has to be fulfilled for admissible cases. The stress derivations for the single energy terms are given in Appendix C.

The thermodynamic forces with respect to a number of internal variables incorporating different damage variables are derived from the Clausius–Duhem inequality condition as

$$Y_{\mathrm{m}}=-\frac{\partial\Psi_{\mathrm{m}}}{\partial D_{\mathrm{m}}},\quad Y_{\mathrm{f}}=-\frac{\partial\Psi_{\mathrm{m}}}{\partial D_{\mathrm{f}}},\quad Y_{\mathrm{int}}=-\frac{\partial\Psi_{\mathrm{int}}}{\partial D_{\mathrm{int}}},\quad A=-\frac{\partial\Psi_{\mathrm{D}}}{\partial\alpha}, \tag{6}$$

where Y_{m}, Y_{f} and Y_{int} are the corresponding damage driving force with respect to matrix damage, fiber damage and interface damage, respectively. A is the thermodynamic driving force associated with the damage strengthening α.

2.3. Free energy density functions

The individual parts of the free energy densities in Eq. (2) are explained in detail, namely those for the matrix Ψ_{m}, the fiber Ψ_{f}, and the matrix-fiber interface Ψ_{int}. The free energy density related to damage strengthening, Ψ_{D}, is not presented here, since the stress, which is the derivative of Ψ with respect to $\mathbf{C}$ according to Eq. (5), does not have a contribution from Ψ_{D} (Ψ_{D} only depends on α, but not on $\mathbf{C}$). However, the damage driving force $A(\alpha)$ affects the damage evolution of the matrix and the interface, and therefore it will be derived later in Section 2.4.

2.3.1. Free energy density function of the matrix

The free energy density function of the matrix is formulated by coupling the hyperelastic behavior with the matrix damage D_{m} following Lemaitre:

$$\Psi_{\mathrm{m}}(\overline{I}_1,J,D_{\mathrm{m}})=[1-D_{\mathrm{m}}]\Psi^0_{\mathrm{m}}. \tag{7}$$

The free energy density of the matrix in the undamaged state Ψ^0_{m} is split into a purely volumetric part $\Psi^0_{\mathrm{m,\,vol}}$ and an isochoric part $\Psi^0_{\mathrm{m,\,iso}}$

$$\Psi^0_{\mathrm{m}}(\overline{I}_1,J)=\Psi^0_{\mathrm{m,\,vol}}(J)+\Psi^0_{\mathrm{m,\,iso}}(\overline{I}_1)$$

$$= \frac{K}{\beta^2}\left[\frac{1}{J^\beta} + \beta \ln J - 1\right] + C_1\left[\exp\left(C_2\left[\bar{I}_1 - 3\right]\right) - 1\right], \tag{8}$$

where K is the bulk modulus and β describes the tension–compression asymmetry behavior. C_1 and C_2 are material parameters in the isochoric part of the strain energy density. Both parts of the energy density have a strictly convex form, and the normalization condition, $\Psi^0_m(\bar{I}_1 = 3, J = 1) = 0$, is satisfied by Eq. (8). The isochoric part is written as an exponential function to reflect the nonlinear deformation behavior of the matrix. The volumetric part follows the function form proposed by Ogden (1972).

The hydrostatic stress of the matrix is derived from the volumetric strain energy function by

$$p_m = \frac{d\Psi^0_{m,\,vol}(J)}{dJ} = \frac{K}{\beta J}\left[1 - \frac{1}{J^\beta}\right]. \tag{9}$$

The tension–compression asymmetry of the normalized hydrostatic stress increases with the increasing β as depicted in Fig. 1.

2.3.2. *Free energy density function of the fiber*

In bio-composites with a staggered alignment of fibers, stresses are transported to the fibers by the interfaces from the matrix – according to the shear-lag model (Gao et al., 2003). Hence, the damage of the interface reduces the stress transported to the fibers in addition to the fiber damage itself. Consequently, the free energy density function of the fiber should account for this coupling, for example, via

$$\Psi_f(D_f, D_{int}, I_4) = [1 - D_{int}][1 - D_f]\Psi^0_f. \tag{10}$$

Following the description of the strain energy stored in the fiber in Holzapfel et al. (2000), the strain energy function of the fiber in the undamaged state Ψ^0_f reads

$$\Psi^0_f = \frac{C_3}{2C_4}\left[\exp\left(C_4[I_4 - 1]^2\right) - 1\right], \tag{11}$$

where C_3 and C_4 are material parameters.

2.3.3. *Free energy density function for fiber–matrix interaction*

The basic idea of the geometric description for fiber–matrix interaction, following Peng Peng et al., 2006, is explained briefly in Appendix B. The free energy contribution from the fiber–matrix interaction is assumed to be related to the relative shear angle between the fiber and the matrix plane, cf. also Peng et al. (2006). As shown in Fig. 2, we define a geometric variable

$$\varphi = \tan^2\theta = \frac{1}{\cos^2\theta} - 1 = \frac{I_4}{I_3}[I_5 - I_1 I_4 + I_2] - 1 \tag{12}$$

to quantify the fiber–matrix shear interaction of composites. The free energy density with respect to the fiber–matrix shear interaction is formulated as

$$\Psi_{int} = [1 - D_{int}]\Psi^0_{int} = [1 - D_{int}]C_{int}\varphi^2, \tag{13}$$

where the undamaged free energy density of the fiber–matrix interaction is defined as $\Psi^0_{int} = C_{int}\varphi^2$. C_{int} accounts for fiber–matrix interaction, and is identified by the micromechanical simulation of the material response under different shear loadings based on a 3D RVE.

2.4. *Damage initiation criteria and evolution laws*

In this section, we introduce criteria for activating the damage process by postulating damage potentials in the thermodynamic force space for three damage modes, i.e., matrix damage, fiber damage and interface debonding. In addition, evolution laws for the damage variables are derived for describing the nonlinear damage accumulation process.

Recalling Eq. (6), the thermodynamic forces associated with the damage variables are derived via the defined strain energy density in the undamaged state as

$$Y_m = \Psi^0_m, \quad Y_f = [1 - D_{int}]\Psi^0_f, \quad Y_{int} = [1 - D_f]\Psi^0_f + \Psi^0_{int}. \tag{14}$$

A strong interaction between interface and matrix damage exists during the damage process in the composites. For instance, the damage of the interface can cause stress concentrations in the matrix, which accelerates the initiation and propagation of matrix damage. In contrast, the fiber is shielded by interface damage; that is, an accelerated damage in the fiber is not caused by the development of interface damage. Therefore, a combined damage potential for matrix and interface damage F^{dam}_{mi} is defined, while an independent damage criterion is applied to the initiation of fiber damage F^{dam}_f. The consistency conditions of the damage potentials must be fulfilled separately in case of active damage evolution:

$$dF^{dam}_{mi} = 0, \quad dF^{dam}_f = 0. \tag{15}$$

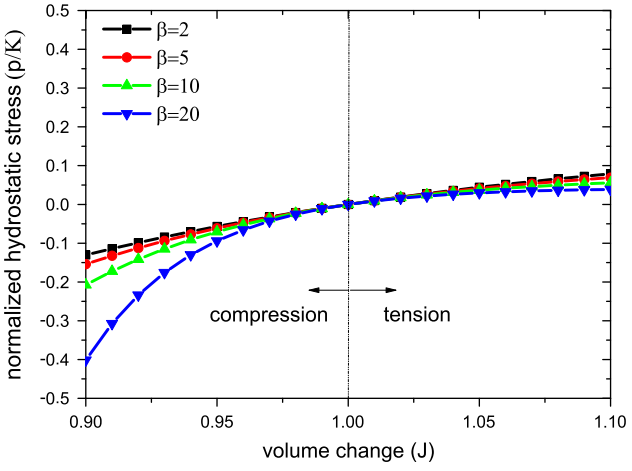

Fig. 1 – Influence of material parameter β on the hydrostatic stress: the tension–compression asymmetry increases with increasing β.

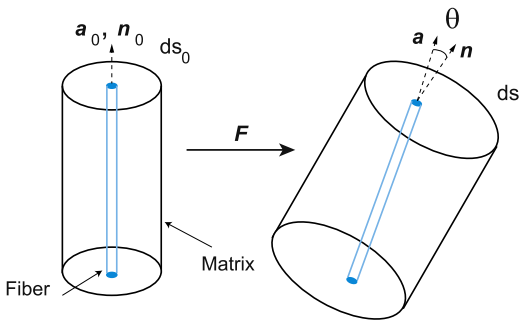

Fig. 2 – Geometric description of the fiber–matrix interaction.

2.4.1. Damage potential of matrix and interface

The damage potential of matrix and interface is proposed as

$$F_{mi}^{dam}(Y_m, Y_{int}, \alpha) = Y_{eq}(Y_m, Y_{int}) - A(\alpha), \tag{16}$$

where the equivalent damage driving force Y_{eq} is defined as

$$Y_{eq} = \sqrt{Y_m^2 + Y_{int}^2} \tag{17}$$

with respect to the interface damage and matrix damage. The consistency condition (15) for this damage potential is written using Eq. (16) as

$$\frac{\partial F_{mi}^{dam}}{\partial Y_{eq}}\dot{Y}_{eq} + \frac{\partial F_{mi}^{dam}}{\partial A}\dot{A} = 0 \Rightarrow \dot{Y}_{eq} - \dot{A} = 0. \tag{18}$$

Damage strengthening α is defined as

$$\dot{\alpha} = \sqrt{\dot{D}_{int}^2 + \dot{D}_m^2}, \quad \alpha = \int \dot{\alpha}\, dt, \tag{19}$$

and an extended exponential evolution law is utilized for its evolution

$$\begin{aligned}\alpha = {} & B_1\left[1 - \exp\left(-b_1\langle Y_{eq}/Y_0 - 1\rangle\right)\right] \\ & + B_2\left[1 - \exp\left(-b_2\langle Y_{eq}/Y_0 - 1\rangle\right)\right],\end{aligned} \tag{20}$$

where $\langle\cdot\rangle$ are the Macauley brackets, i.e., $\langle x\rangle = [|x| + x]/2$. The double terms formulation provides a more accurate prediction of damage evolution process; however, at the expense of introducing more material parameters. The material parameters B_i, b_i and Y_0 with $i = 1, 2$ are identified by the stress–strain curve under tensile loading. Furthermore, the initial damage threshold Y_0 could be different under tensile and compressive loading. Therefore, Y_0^{ten} and Y_0^{com} are used for tension ($p_m > 0$) and compression ($p_m \le 0$), respectively.

By taking the time derivative of Eq. (20), the rate form of damage strengthening is derived as $\dot{\alpha} = (\partial\alpha/\partial Y_{eq})\dot{Y}_{eq}$. Using the relationship between the rate of damage resistance and the rate of the equivalent damage driving force, $\dot{A} = \dot{Y}_{eq}$, Eq. (18), the evolution of damage resistance $\dot{A}$ is related with the evolution of damage strengthening as

$$\dot{A} = \frac{Y_0}{B_1 b_1 \exp\left(-b_1\left\langle\frac{Y_{eq}}{Y_0} - 1\right\rangle\right) + B_2 b_2 \exp\left(-b_2\left\langle\frac{Y_{eq}}{Y_0} - 1\right\rangle\right)}\dot{\alpha}, \tag{21}$$

hence,

$$\frac{\partial A}{\partial \alpha} = \frac{Y_0}{B_1 b_1 \exp\left(-b_1\left\langle\frac{Y_{eq}}{Y_0} - 1\right\rangle\right) + B_2 b_2 \exp\left(-b_2\left\langle\frac{Y_{eq}}{Y_0} - 1\right\rangle\right)}. \tag{22}$$

2.4.2. Damage potential of the fiber

The damage potential of fiber is given as

$$F_f^{dam}(Y_f, D_f) = Y_f - Z(D_f), \tag{23}$$

where the damage resistance Z of fiber is a function of the fiber damage D_f. The following exponential damage evolution law is used for modeling the damage evolution process of the fiber,

$$D_f = 1 - \exp\left(-b_3\left\langle\frac{Y_f}{Y_{cf}} - 1\right\rangle\right), \tag{24}$$

where Y_{cf} determines the strength of the fiber. The evolution of the damage resistance of the fiber is derived by taking the time derivative of Eq. (24) and using the consistency condition $\dot{Y}_f = \dot{Z}$

$$\dot{Z} = Y_{cf} b_3 \exp\left(b_3\left\langle\frac{Y_f}{Y_{cf}} - 1\right\rangle\right)\dot{D}_f. \tag{25}$$

In general, the strength of the material is different under tensile and compression loading. Therefore, the critical energy of the fiber Y_{cf} depends on the loading mode:

$$Y_{cf} = \begin{cases} Y_{cf}^{ten} & I_4 \ge 1 \\ Y_{cf}^{com} & I_4 < 1 \end{cases}, \tag{26}$$

where Y_{cf}^{ten} and Y_{cf}^{com} are the critical energies of the fiber under tension and compression, respectively.

2.4.3. Damage evolution laws

The evolution of internal variables are deduced by the normality rule based on the defined damage dissipation potentials

$$\dot{D}_m = \dot{\lambda}_{mi}\frac{\partial F_{mi}^{dam}}{\partial Y_m}, \quad \dot{D}_{int} = \dot{\lambda}_{mi}\frac{\partial F_{mi}^{dam}}{\partial Y_{int}}, \quad \dot{D}_f = \dot{\lambda}_f\frac{\partial F_f^{dam}}{\partial Y_f}. \tag{27}$$

Here, $\dot{\lambda}_{mi}$ and $\dot{\lambda}_f$ are damage multipliers with respect to the damage potential functions F_{mi}^{dam} and F_f^{dam}, respectively. Considering the proposed damage potentials, Eq. (27) simplifies to

$$\dot{D}_m = \dot{\lambda}_{mi}\frac{Y_m}{Y_{eq}}, \quad \dot{D}_{int} = \dot{\lambda}_{mi}\frac{Y_{int}}{Y_{eq}}, \quad \dot{D}_f = \dot{\lambda}_f. \tag{28}$$

$\dot{\lambda}_{mi} = \dot{\alpha}$ follows from Eq. (28) with Eq. (19).

The consistency conditions of the damage potential functions in Eq. (15) are used in the following to solve the multipliers $\dot{\lambda}_f$ and $\dot{\lambda}_{mi}$.

Matrix and interface: Using Eq. (17), the consistency condition Eq. (18) is reformulated as

$$\frac{Y_m}{Y_{eq}}\dot{Y}_m + \frac{Y_{int}}{Y_{eq}}\dot{Y}_{int} - \frac{\partial A}{\partial \alpha}\dot{\alpha} = 0, \tag{29}$$

where $\frac{\partial A}{\partial \alpha}$ is taken from Eq. (22). Substituting the time derivatives of Eq. (14) into above equation, yields

$$\frac{Y_m}{Y_{eq}}\dot{\Psi}_m^0 + \frac{Y_{int}}{Y_{eq}}\left[[1 - D_f]\dot{\Psi}_f^0 + \dot{\Psi}_{int}^0 - \Psi_f^0\dot{D}_f\right] - \frac{\partial A}{\partial \alpha}\sqrt{\dot{D}_{int}^2 + \dot{D}_m^2} = 0. \tag{30}$$

Applying the damage evolution equation (27) for $\dot{D}_m$, $\dot{D}_{int}$ and $\dot{D}_f$, one can write

$$\frac{Y_m}{Y_{eq}}\dot{\Psi}_m^0 + \frac{Y_{int}}{Y_{eq}}\left[[1 - D_f]\dot{\Psi}_f^0 + \dot{\Psi}_{int}^0 - \Psi_f^0\dot{\lambda}_f\right] - \frac{\partial A}{\partial \alpha}\dot{\lambda}_{mi} = 0. \tag{31}$$

Fiber: Analogically, the consistency condition $dF_f^{dam} = 0$ is reformulated as

$$[1 - D_{int}]\dot{\Psi}_f^0 - \Psi_f^0\frac{Y_m}{Y_{eq}}\dot{\lambda}_{mi} - \frac{\partial Z}{\partial D_f}\dot{\lambda}_b = 0, \tag{32}$$

where $\frac{\partial Z}{\partial D_f} = Y_{cf} b_3 \exp\left(b_3\langle\frac{Y_f}{Y_{cf}} - 1\rangle\right)$ follows from Eq. (25).

Combing Eqs. (31) and (32), the unknowns in the damage evolution equations $\dot{\lambda}_f$ and $\dot{\lambda}_{mi}$ are solved simultaneously. Then, the rate of damage variables is computed by Eq. (28).

Damage interaction: In the proposed damage model, three damage variables are used for representing different damage mechanisms in dental enamel. The interaction between them is taken into account by using the combined damage potential of matrix and interface. Furthermore, both damages D_f and D_{int} are coupled in the fiber hyperelastic energy. In

addition, the material is assumed to not entirely fail as one damage variable reaches a critical state. On the other hand, the other damage mechanisms should be influenced and the damage accumulation process is accelerated. To this end, a common critical damage value $D_c \leq 1$ is defined for the three damage variables.

If one damage variable of interface damage or matrix damage D_i with $i = \{\text{int}, \text{m}\}$ reaches the critical state, $D_i = D_c$, the damage evolution process of the other damage variable D_j is accelerated

$$D_j = D_j^c + \omega K_c \left[Y_j - Y_j^c \right] \tag{33}$$

where D_j^c, Y_j^c and $K^c = \frac{dD_j}{dY_j}\Big|_c$ are the current damage value, damage driving force and the tangent of damage evolution rate of damage variable D_j at the state $D_i = D_c$. ω is the influence factor that accelerates the damage evolution process.

In the case of total failure of fibers, $D_f = D_c$, the parameters $b_i (i = \{1, 2\})$ in the damage evolution equation of D_{int} and D_m are replaced by ωb_i.

3. Micromechanical model of dental enamel

The material response of the composite under tension, compression and shear loading is investigated by a micromechanical model with a 3D, periodic RVE which explicitly takes into account the spatial distribution of the fibers, matrix and interfaces.

3.1. *Setup of the 3D RVE model*

Dental enamel has three hierarchical levels: nano-fibers surrounded by a thin protein layer (intra-rod, level 1), multiple rods of fibers, again surrounded by a protein layer (inter-rod, level 2), and decussating bundles of rods located near the dentin (Hunter-Schreger bands, level 3). The first and second hierarchical levels are illustrated in Fig. 3. On level 1, the composite is composed of approx. 90% of hard hydroxyapatite nano-fibers which are regarded to be unidirectionally aligned in the protein matrix. Due to the small size and the complex arrangement of the fibers, no substantiated information about the length of the fibers is available. A finite length and the discontinuity of the nano-fibers are assumed based on the presence of the initial defects: the fibers most probably have weak spots, flaws or imperfections which are a result, e.g., of biomineralization. These are visible at the first hierarchical level under high resolution electron microscopy as shown in Fig. 3. In order to simplify the RVE and reduce the computational cost without loss of essential information, we assume that the nano-fibers are periodically arranged in a staggered manner and represented by prisms with a hexagonal cross-section as shown in Fig. 4.

The fibers are aligned in z-direction. The side length S of the hexagon and thickness t of the protein layer are 29 nm and 2 nm, respectively. Accordingly, the width W and the thickness H of the RVE are 165 nm and 95 nm, respectively. In order to investigate the influence of the aspect ratio of the mineral fiber on the overall elastic behavior of composite, the length L of the RVE varies from 290 nm to 3364 nm. The aspect ratio of fibers $\rho = L/2S$ varies from 5 to 58.

The simulations of all RVE models are performed with ABAQUS/Standard within the framework of finite deformation. More than 45,000 linear cubic elements (C3D8) are used and meshes were checked to be a converged finite element discretization for obtaining accurate simulation results without mesh-dependence. Periodic boundary conditions are applied.

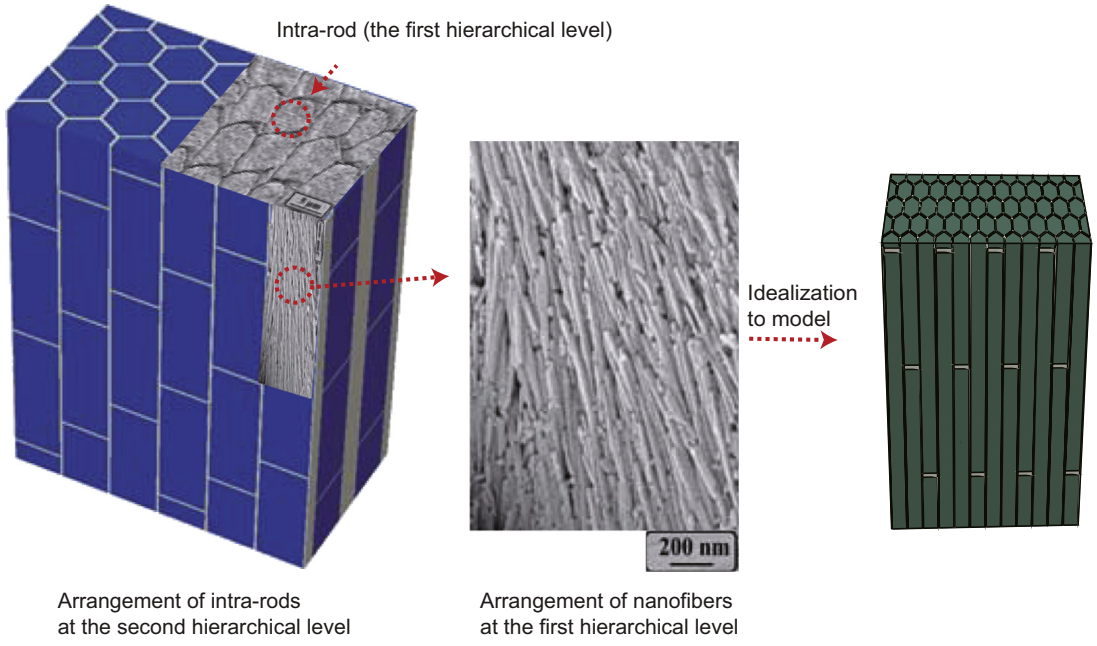

Fig. 3 – 3D RVE with periodic structure. Staggered aligned mineral fibers and protein.

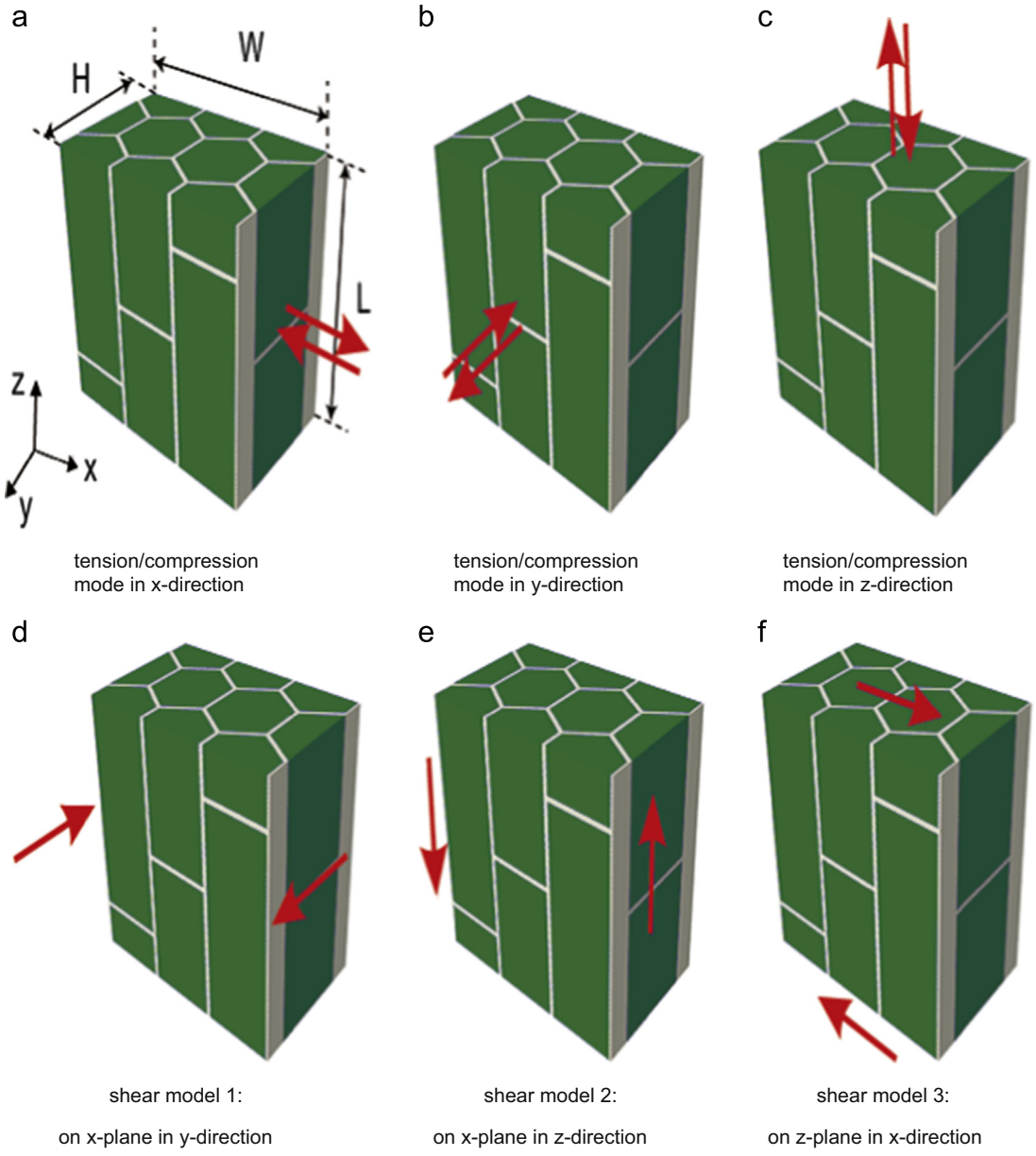

Fig. 4 – 9 load cases for the validation of the proposed anisotropic hyperelasticity model at the first hierarchical level without considering damage effect.

3.2. *Load cases*

We investigate 9 loading cases for verifying the hyperelastic behavior of the proposed constitutive model, including uniaxial tension and compression in three different directions, shear in the transverse plane, shear along fiber direction, shear perpendicular to the fiber direction (see Fig. 4). Shearing perpendicular to the fiber direction (shear mode 3) induces an additional stretch of the fiber, in contrast to shear along the fiber direction (shear mode 2).

The average deformation gradient $\overline{\mathbf{F}}$ applied to the RVE has to satisfy

$$\overline{\mathbf{F}} = \frac{1}{V_0}\int_{V_0} \mathbf{F}(\mathbf{X})d\mathbf{X}. \tag{34}$$

The corresponding macroscopic deformation gradient $\overline{\mathbf{F}}$ for each loading mode is written as

$$\overline{\mathbf{F}}^{xx} = \begin{bmatrix} \kappa & 0 & 0 \\ 0 & 1 & 0 \\ 0 & 0 & 1 \end{bmatrix}, \quad \overline{\mathbf{F}}^{yy} = \begin{bmatrix} 1 & 0 & 0 \\ 0 & \kappa & 0 \\ 0 & 0 & 1 \end{bmatrix}, \quad \overline{\mathbf{F}}^{zz} = \begin{bmatrix} 1 & 0 & 0 \\ 0 & 1 & 0 \\ 0 & 0 & \kappa \end{bmatrix},$$
$$\overline{\mathbf{F}}^{xy} = \begin{bmatrix} 1 & \kappa & 0 \\ 0 & 1 & 0 \\ 0 & 0 & 1 \end{bmatrix}, \quad \overline{\mathbf{F}}^{zx} = \begin{bmatrix} 1 & 0 & 0 \\ 0 & 1 & 0 \\ \kappa & 0 & 1 \end{bmatrix}, \quad \overline{\mathbf{F}}^{xz} = \begin{bmatrix} 1 & 0 & \kappa \\ 0 & 1 & 0 \\ 0 & 0 & 1 \end{bmatrix}. \tag{35}$$

The overall behavior of the composite is deduced from the relations between the average of the resulting stress field and these boundary conditions. The average of the stress field is determined from the traction acting on the boundaries of the RVE. The average 1. Piola–Kirchhoff stress $\overline{\mathbf{P}}$ is obtained as

Table 1 – Summary of material parameters for three different aspect ratios.

Aspect ratio $\rho = 5$:			
$C_1 = 289.4$ MPa;	$C_2 = 11.78$;	$C_3 = 4563$ MPa	$C_4 = 4.54$
$C_{int} = 10,186$ MPa	$K = 9805$ MPa	$\beta = 20$	
Aspect ratio $\rho = 10$:			
$C_1 = 289.4$ MPa;	$C_2 = 11.78$;	$C_3 = 7829$ MPa	$C_4 = 1.29$
$C_{int} = 15,303$ MPa	$K = 9805$ MPa	$\beta = 20$	
Aspect ratio $\rho = 58$:			
$C_1 = 289.4$ MPa;	$C_2 = 11.78$;	$C_3 = 11,488$ MPa	$C_4 = -2.4$
$C_{int} = 19,070$ MPa	$K = 9805$ MPa	$\beta = 20$	

$$\overline{\mathbf{P}} = \frac{1}{V}\int_V \mathbf{P}(\mathbf{X})d\mathbf{X}. \tag{36}$$

Using the equilibrium equations and the divergence theorem, the average nominal stress $\overline{\mathbf{P}}$ is computed with the reaction force of the auxiliary dummy nodes of each face. The average Cauchy stress of the RVE is calculated by $\overline{\boldsymbol{\sigma}} = J^{-1}\overline{\mathbf{P}} \cdot \overline{\mathbf{F}}^T$.

4. Simulation of the anisotropic hyperelastic behavior

In the RVE simulations, an Arruda–Boyce hyperelastic model is used to simulate the nonlinear deformation behavior of the protein, while the deformation behavior of the fibers are represented by a Neo-Hooke hyperelastic model. The details of these constitutive models are given in Bargmann et al. (2013).

The material parameters in the hyperelastic part of the proposed model are identified by adjusting the analytical solution for the anisotropic model to the numerical results of the micromechanical model subjected to four loading conditions: deformation κ of shearing in the transverse plane, tension in fiber direction, compression in transverse direction and shearing along the fiber direction. The details of the identification procedure of the material parameters are found in Appendix D. The material parameters of the anisotropic hyperelastic model are listed in Table 1 for three different aspect ratios.

The comparison between the simulation results of the RVE and the homogenized hyperelastic model is shown in Fig. 5 in terms of the Cauchy stress vs. logarithmic strain. The symbols in the figures represent the simulation results of the RVE model, while the solid lines denote the results using the analytical expressions of the Cauchy stresses in the anisotropic homogenized hyperelastic model. Whereas the RVE simulations take several hours of computation time, the solution of the anisotropic hyperelastic theory is calculated within seconds.

4.1. *Tension and compression response*

The tension and compression behavior is studied in the strain range from −10% to 10% strain.[1] Both, the average tension and compression behavior in all loading directions are accurately predicted by the present hyperelastic model with the material parameters identified in the previous section. Further, the material response in the two transverse directions x and y are nearly identical, justifying the use of a transversely isotropic hyperelastic model.

As shown in Fig. 5a, c, and e, the material behaves stiffer under compression than under tension loading. The difference in transverse direction is apparent for all aspect ratios, while the difference in fiber direction decreases with the aspect ratio due to the additional stiffening effect of the fiber. In order to understand these deformation mechanisms of the composite, the distributions of the logarithmic strain are shown in Fig. 6 for the composite with aspect ratio $\rho = 10$ at a macroscopic average strain 8% in 6 different load cases, namely tension and compression in three directions.

Under transverse tensile loading, the logarithmic strain of the protein layer is less than 0.5 at a macroscopic average elongation of 8%, while it exceeds 1.5 at a same average strain level under transverse compression. This is due to the fact that the deformation of the composite is induced by the soft protein layer under transverse loading. Furthermore, the thin protein layer and the high fiber volume fraction result in quite different strains of the protein layer under transverse tension and compression. The deformation mechanism under loading in fiber direction is different: the logarithmic strain of the protein layer exceeds 1.0 at a macroscopic elongation of 8% for both tension and compression loading cases, since the load between mineral fibers is transmitted by the shear deformation of protein layer parallel to fiber direction. In other words, the tension–compression asymmetry results from the unique microstructural features of dental enamel, i.e., the staggered alignment of fibers surrounded by an extremely thin soft protein layer of only a few nanometers.

4.2. *Shear response*

The simulation results of the shear loading cases are depicted in Fig. 5b, d and f. Generally, the stress–strain curves in all shear loading cases are accurately predicted by the present hyperelastic model. In the case of transverse shear (shear mode 1), fiber–matrix interaction is not activated during the deformation. Therefore, the stress is significantly lower compared to the other two shear modes. Furthermore, transverse shear is independent of the aspect ratio of fiber. In addition, the shear stress for the case of longitudinal shear (shear mode 2, Fig. 4e) is slightly lower than for shear in the plane perpendicular to the fiber direction (shear mode 3, Fig. 4f), since an additional stretch of fiber occurs in the latter.

The shear stress contours for all 3 shear loading modes are shown in Fig. 7 for aspect ratio $\rho = 10$ at the macroscopic shear strain level 20%. It is seen that the shear stress value in the fiber for shear mode 1 is lower than the other two shear modes at identical load levels. This difference indicates a significant fiber–matrix interaction during the deformation process for the latter.

In order to study the influence of the fiber–matrix interaction on the deformation behavior under different shear modes, the fraction of the free energy density induced by

[1] The maximum fracture strain is about 8% during micropillars testing of dental enamel in multiple directions (Yilmaz et al., 2015).

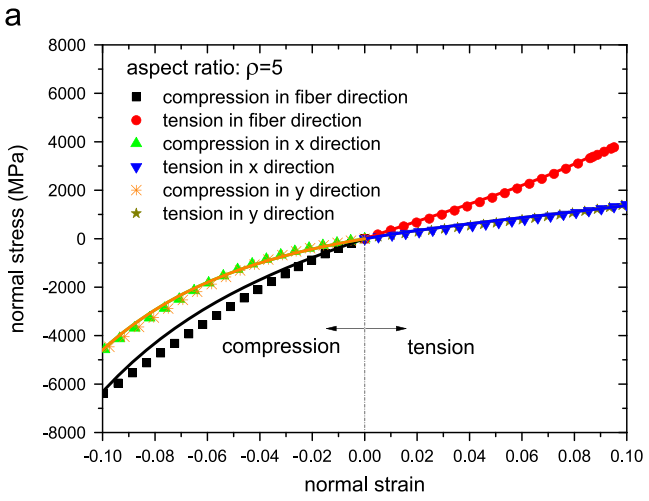

$\rho = 5$: uniaxial tension and compression

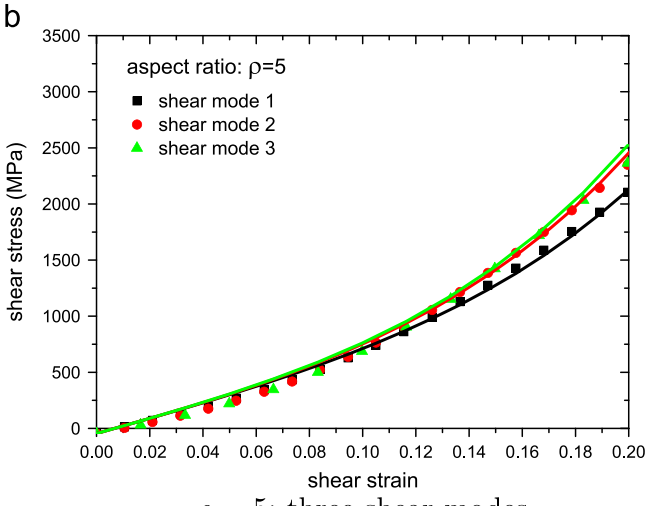

$\rho = 5$: three shear modes

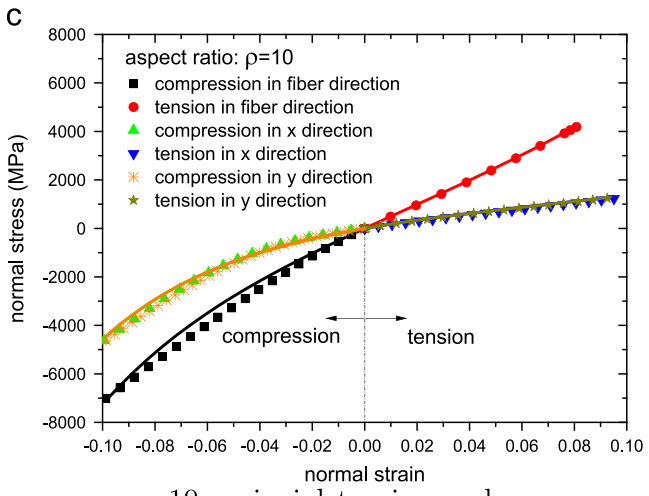

$\rho = 10$: uniaxial tension and compression

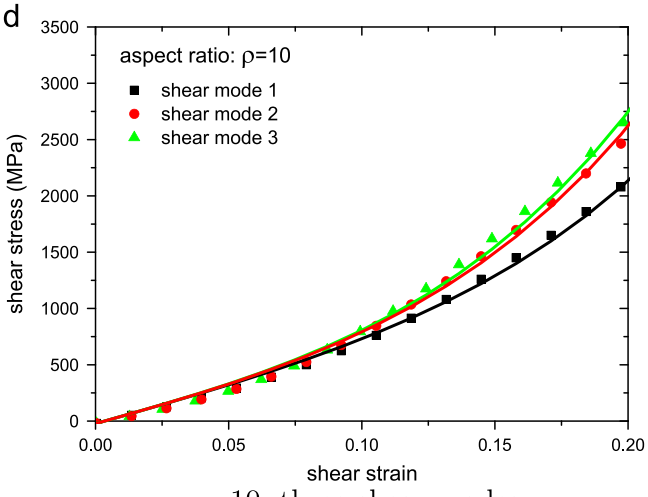

$\rho = 10$: three shear modes

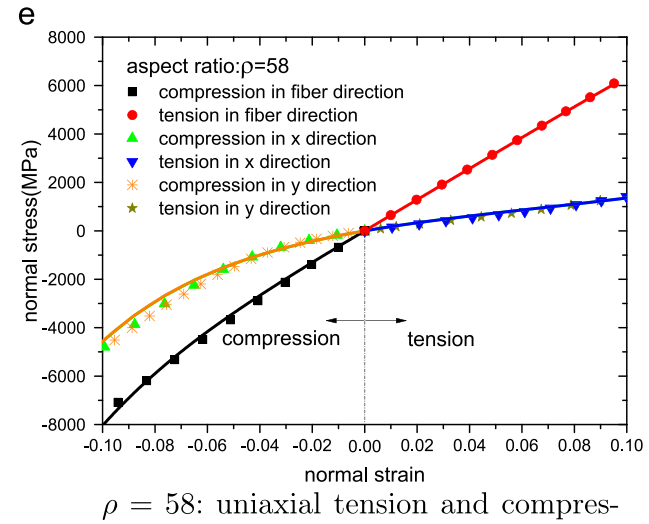

$\rho = 58$: uniaxial tension and compression

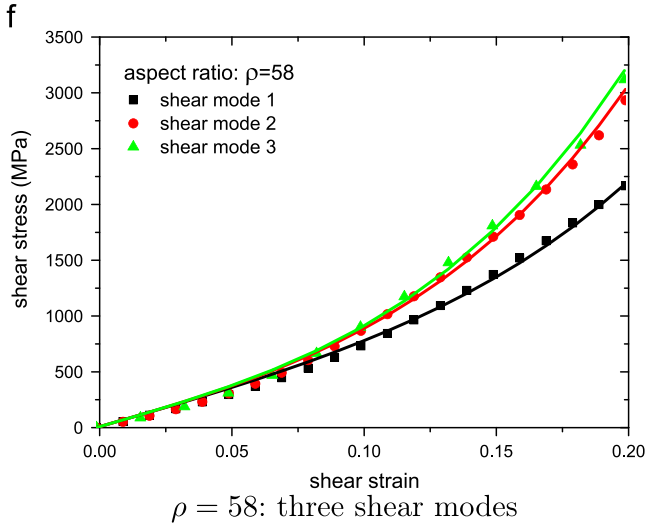

$\rho = 58$: three shear modes

Fig. 5 – Comparison of the overall stress-logarithmic strain response between the anisotropic hyperelastic model (solid lines) and the micromechanical simulations of the RVE (symbols) with three different aspect ratio under various loading conditions. The present anisotropic hyperelastic model provides a suitable description of hyperelastic behavior of dental enamel.

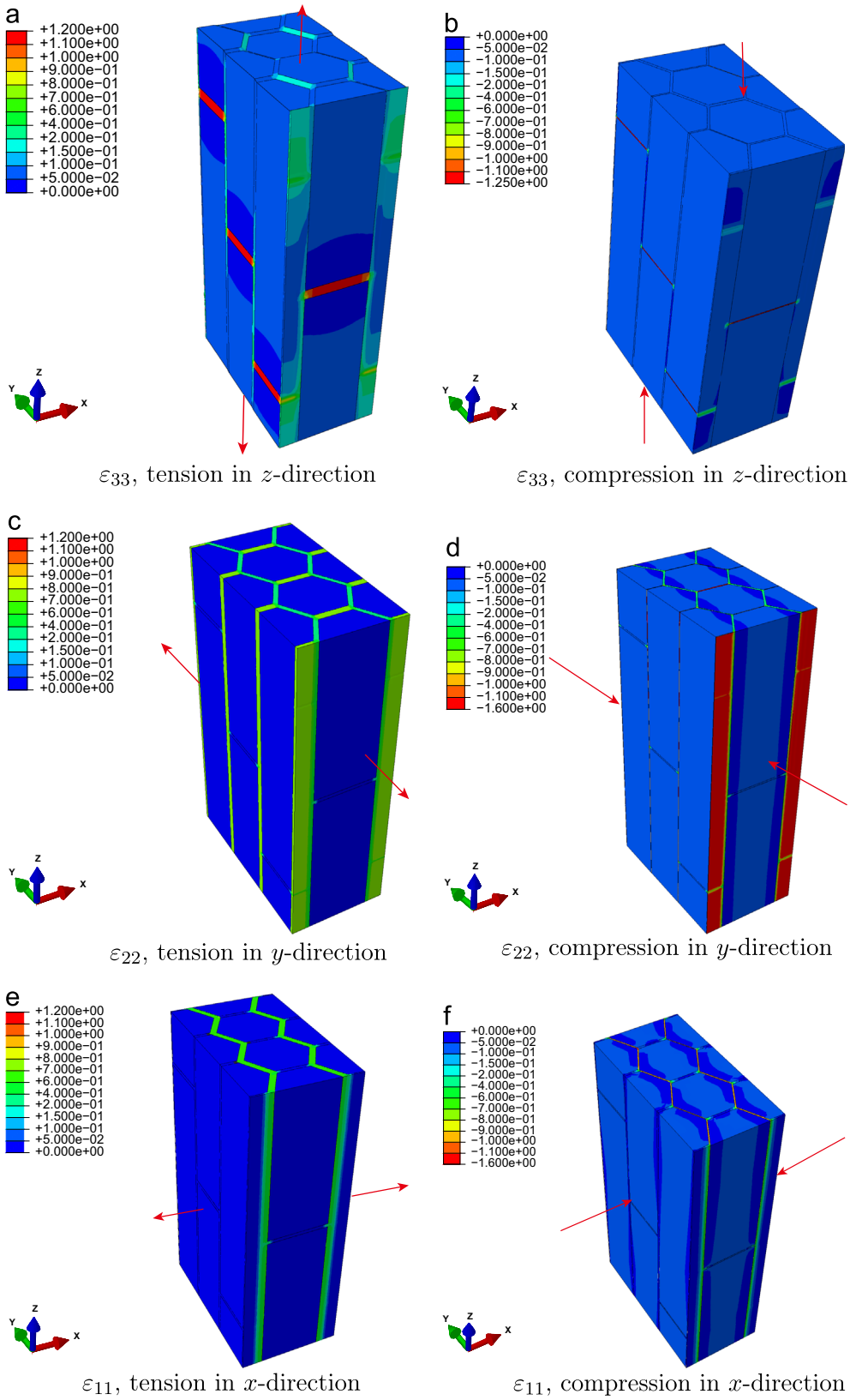

Fig. 6 – Strain distribution in loading direction at a macroscopic average strain of 8%. 6 different loading cases incorporating tension and compression for the composite with the aspect ratio $\rho = 10$. Tension and compression asymmetry results from different deformation mechanisms.

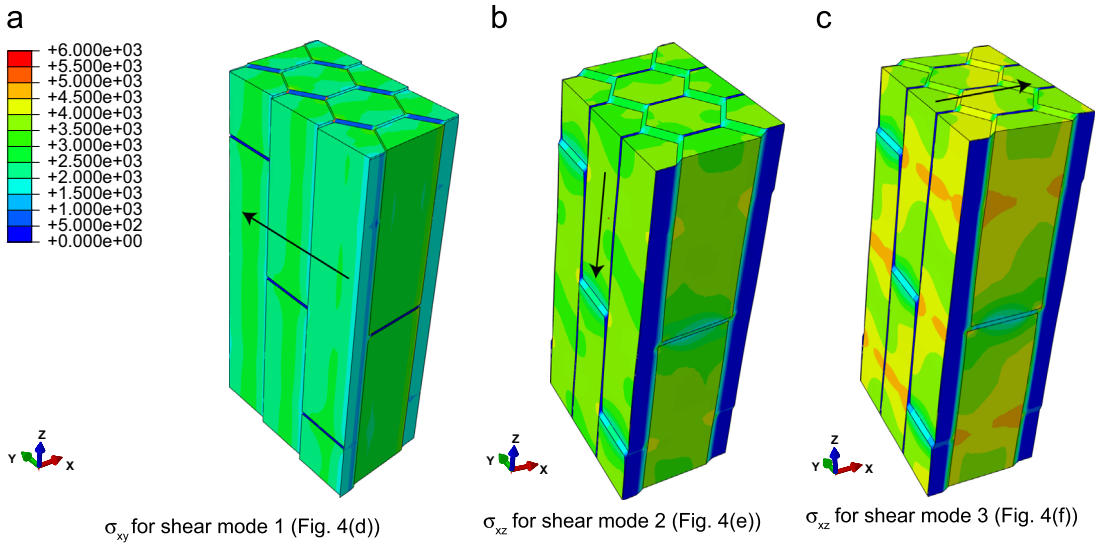

Fig. 7 – Shear stress distribution. Aspect ratio $\rho = 10$. 3 different shear loadings. The simulation results indicate that more fiber–matrix interaction is present for shear modes 2 and 3.

fiber–matrix interaction $\frac{\Psi^0_{\text{int}}}{\Psi^0_{\text{total}}}$ is plotted in Fig. 8 for different aspect ratios. The total free energy density is defined as $\Psi^0_{\text{total}} = \Psi^0_{\text{m}} + \Psi^0_{\text{f}} + \Psi^0_{\text{int}}$. The simulation results clearly show that the fiber–matrix interaction plays an important role in the deformation behavior under shear mode 2 and 3. For shear mode 1, no fiber–matrix interaction occurs. The shear interaction is more prominent for high aspect ratios: in case of a composite with $\rho = 58$, $\frac{\Psi^0_{\text{int}}}{\Psi^0_{\text{total}}}$ is nearly 20%.

The validation of the proposed hyperelastic model under different shear loadings confirms that the effect of fiber-interaction on deformation behavior of the dental enamel is captured by the present fiber–matrix interaction function.

5. Simulation of damage behavior of the dental enamel

Based on the previous results, the present anisotropic hyperelastic model is extended to simulate the damage behavior of dental enamel.

5.1. *Damage modeling in the micromechanical simulation*

The (homogenized) anisotropic damage model is compared to the micromechanical damage models proposed in Ma et al. (2016). The interface between protein and mineral is modeled by the same cohesive zone model that has previously been used in Scheider et al. (2015), since this is the most appropriate model for physical interfaces. The constitutive model for the material separation is based on a bi-linear traction separation law, which is defined by two parameters for each direction, the cohesive strength T_0 and the fracture energy Γ_0. The critical separation, at which the interface has completely failed, δ_c, is then given by $\delta_c = 2\Gamma_0/T_0$.

Identical material parameters for the first hierarchical composite of dental enamel as used in Ma et al. (2016) are employed for the fiber, matrix and interface damage in the present micromechanical simulations. The resulting

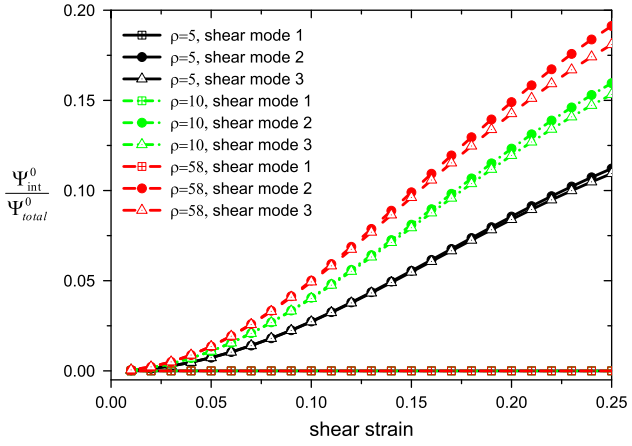

Fig. 8 – Fraction of fiber–matrix interaction free energy density for aspect ratios 5, 10 and 58 under different shear loadings. The fiber–matrix interaction significantly influences the deformation behavior of dental enamel under shear loadings.

strengths of fiber and matrix in the continuum damage model are 2000 MPa and 200 MPa, respectively. Furthermore, the strength and fracture energy of interface between fiber and matrix are $T_0 = 60$ MPa and $\Gamma_0 = 1.5$ J/m^2, respectively. For detailed information the interested reader is referred to Scheider et al. (2015) and Ma et al. (2016).

5.2. *Parameter identification of the anisotropic damage model*

In addition to the hyperelastic part identified in the previous section, the material parameters of damage initiation and evolution in the proposed damage model are to be calibrated. For this purpose, the same 3D RVE is subjected to uniaxial tension loading in the fiber direction. In dental enamel, it is found that the main damage mechanism is closely related to

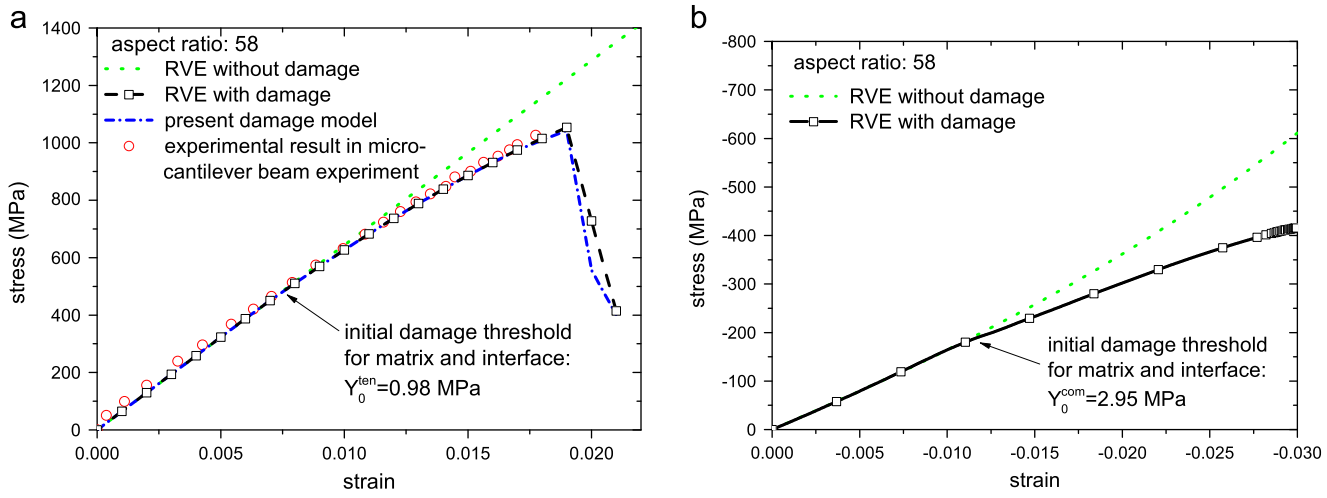

Fig. 9 – Comparison of stress–strain curves from the experiment, micromechanical simulation and the anisotropic damage model for the composite with the aspect ratio $\rho = 58$; (a) stress–strain curves under tension in fiber direction, (b) stress–strain curves from micromechanical simulations under compression in transverse direction for identifying the initial damage threshold Y_0^{com}.

the aspect ratio of the mineral fiber (Bechtle et al., 2012). Therefore, it is necessary to study the applicability of the proposed damage model for different aspect ratios which involve different damage mechanisms. Two aspect ratios $\rho = 10$ and $\rho = 58$ are selected for studying the damage process of the bio-composites. We have previously shown in Ma et al. (2016) that the failure mechanism differs significantly between these aspect ratios.

5.2.1. *Composite with a high aspect ratio*

In Fig. 9, the homogenized tension stress–strain curve obtained from the micromechanical simulation including damage is denoted by black symbols for the composite with aspect ratio $\rho = 58$. The numerical results are compared to the experimental data from micro-cantilever beam testing (Bechtle et al., 2012), showing that the micromechanical simulation results are in good accordance with the experimental result.

The initial damage threshold of matrix and interface, Y_0, is directly calculated at the strain level of damage initiation, which is determined by comparing the simulated stress–strain curves from the RVE simulations with and without damage. The damage initiation of matrix and interface is found at $\varepsilon = 0.007$, which gives $Y_0^{ten} = 0.98$ MPa. The critical damage resistance of fiber Y_{cf}^{ten} is adjusted based on the strain at damage initiation of the fiber. Since the fiber is brittle, this point corresponds to the point of maximum stress. For a high aspect ratio, it is found that a single exponential function for α (Eq. (20)) is sufficient to describe the damage evolution process, since the damage of the interface and matrix develops gradually in this case. Therefore, $B_2 = 0$ is set and only five parameter are left for the identification (b_2 has no effect if B_2 is zero). The material parameters b_1 and B_1 are obtained by iteratively fitting the stress–strain curve from the micromechanical simulation. The initial damage threshold of matrix and interface under compression $Y_0^{com} = 2.95$ MPa is identified based on stress–strain curves from micromechanical simulations under compression in transverse direction, which is different from the value under tension Y_0^{ten}. The identified material parameters are listed in Table 2 for the composite with aspect ratio $\rho = 58$.

Table 2 – Material parameters in damage model for composite with high aspect ratio $\rho = 58$.

$b_1 = 0.025$,	$b_3 = 2.0$,	$B_1 = 1.0$,	$B_2 = 0.0$,
$Y_0^{ten} = 0.98$ MPa,	$Y_0^{com} = 2.95$ MPa,	$Y_{cf}^{ten} = 7.2$ MPa	

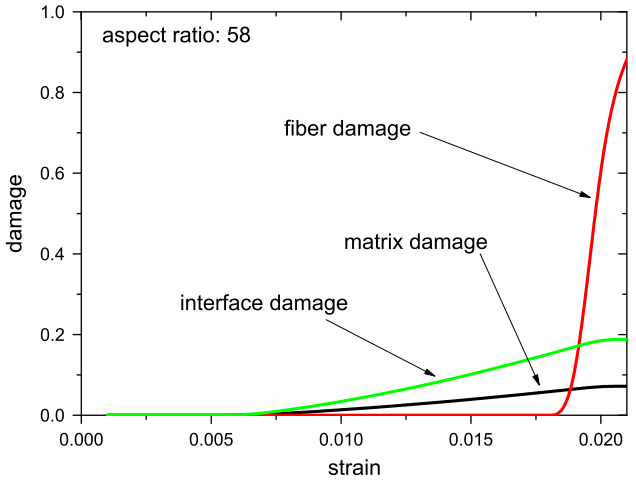

Fig. 10 – Damage evolution process calculated by the anisotropic damage model for aspect ratio $\rho = 58$. The interface damage develops more rapidly than matrix damage and dominates for the degradation process of material until the fiber damage is activated.

In the anisotropic damage model, the different damage mechanisms are distinguished. Therefore, the specific damage evolution curves from the simulation for fiber,

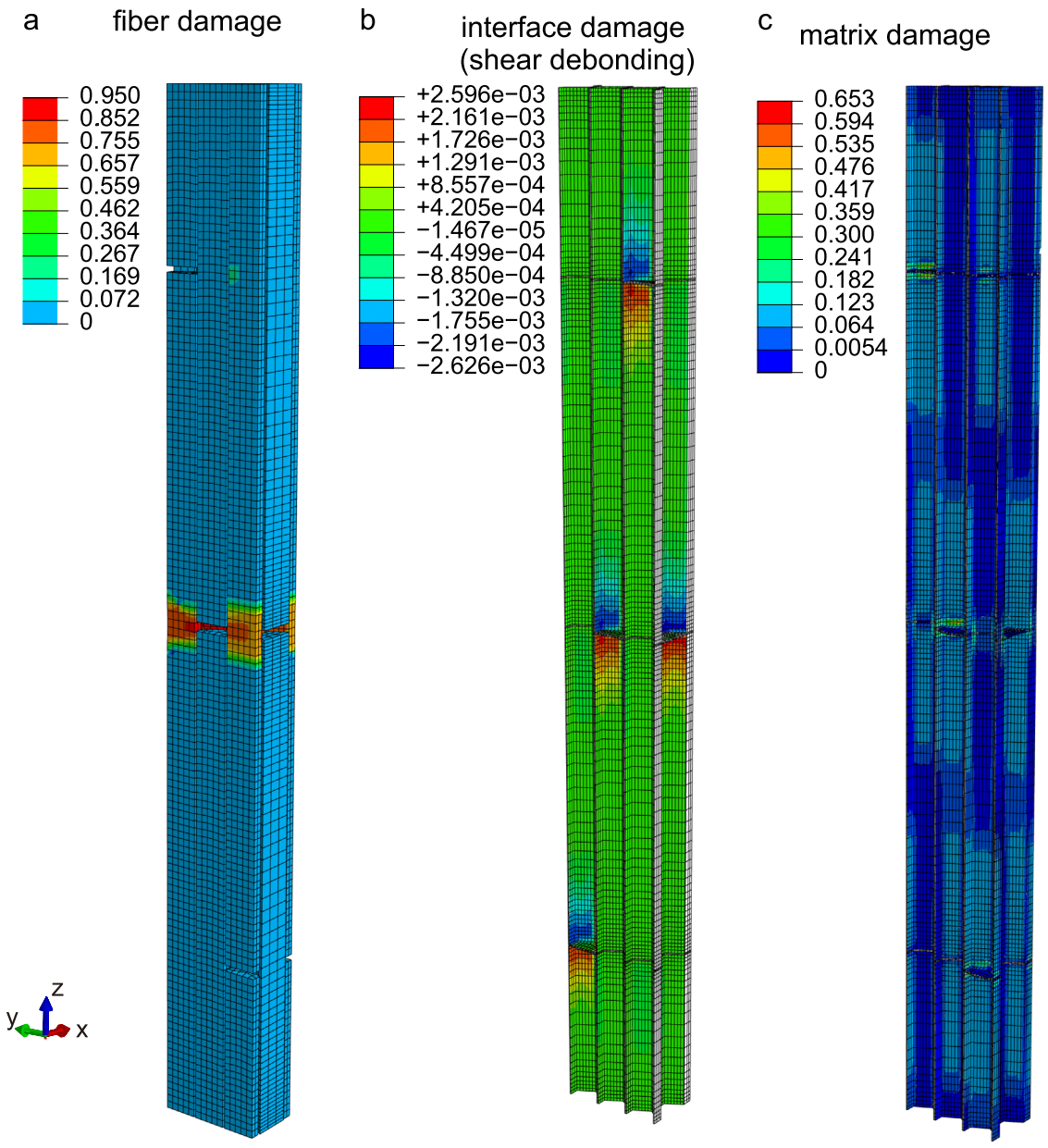

Fig. 11 – Damage distribution within the RVE with aspect ratio $\rho = 58$ at end of simulation: (a) in the fiber, (b) at the interface (cohesive separation), (c) in the matrix. Three damage mechanisms are activated, but eventually the fiber damage in the middle of the RVE leads to the breaking of the composite.

matrix and interface are displayed separately in Fig. 10. Under tensile loading in fiber direction, the matrix and interface damage initiate simultaneously at the strain level 0.7%. The interface damage develops more rapidly than matrix damage and dominates for the degradation process of material until fiber damage is activated. Once the loading reaches a critical state, the fiber damage is activated and leads to a rapid loss of loading bearing capacity of the composite, which results in the failure of the composite.

The development of multiple damage variables computed by the anisotropic damage model has to be consistent with the computational results of the micromechanical simulation. Considering the micromechanical simulation results, the fiber, interface and matrix damage distribution at an average strain level of 2% are shown in Fig. 11a, b and c, respectively. It is observed that all three damage mechanisms are activated and fiber damage in the middle of the RVE leads to the breaking of the composite. The zones of interface damage are mainly located near the fiber ends. The interface perpendicular to the loading direction (at the fiber ends) is significantly separated and damaged. It is indicated that the interface damage has a higher value than matrix damage. These observations in the micromechanical simulation confirm that the damage evolution process of the composite with a higher aspect ratio is captured by the proposed anisotropic damage model.

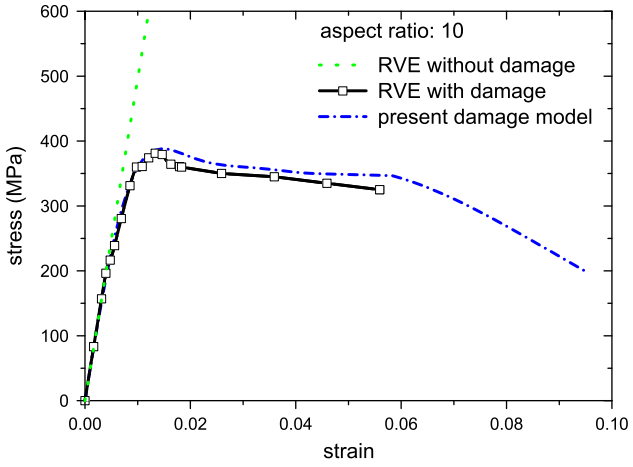

Fig. 12 – Comparison of stress–strain curves from the micromechanical simulation and the anisotropic damage model for the composite with aspect ratio $\rho = 10$. The proposed damage model with these material parameters provides a reasonable prediction.

Table 3 – Material parameters in the damage model for the composite with aspect ratio $\rho = 10$.

$b_1 = 0.255$,	$b_2 = 0.036$,	$B_1 = 0.775$,	$B_2 = 0.383$,
$Y_0^{ten} = 0.6$ MPa,	$Y_0^{com} = 2.95$ MPa		

5.2.2. *Composite with a low aspect ratio*

In specimen with a low aspect ratio, interface and matrix damage are dominating the failure of the composites (Yilmaz et al., 2015; Bargmann et al., 2013). In order to provide a proper constitutive description for composites with different microstructures, the applicability of the proposed damage model to the composite with shorter fibers is investigated using the composite with aspect ratio $\rho = 10$.

The stress–strain relationship from the RVE simulation is illustrated by black symbols in Fig. 12. The identical strategy for identifying the material parameters is applied to the composite with aspect ratio $\rho = 10$. The damage initiation of matrix and interface for this composite under tension is found $Y_0^{ten} = 0.62$ MPa. Since the material response in transverse direction is independent of the aspect ratio, Y_0^{com} equals the value of the composite with a large aspect ratio. In specimens with small aspect ratios fiber breaking does not occur, hence, the parameter Y_{cf}^{ten} is set larger than the value according to the maximum experienced stress of the fiber, which leads to the absence of fiber damage. The set of material parameters for the anisotropic damage model is summarized in Table 3. In general, the proposed damage model with these material parameters provides a reasonable prediction in the stress–strain response of the composite with a low aspect ratio under tensile loading.

The damage evolution curves computed by the proposed anisotropic damage model are displayed in Fig. 13a. In contrast to the composite with a high aspect ratio, the fiber damage is not activated in the composite with a low aspect ratio due to the higher value of Y_{cf}^{ten}, which matches the stress distribution in the micromechanical analysis shown in Fig. 13b. It is seen that the stress level in the fiber is much lower than the strength of fiber. The interface and matrix damage distributions are illustrated in Fig. 13c and f, respectively. Compared to the interface and matrix damage distributions in the composite with $\rho = 58$, the interface and matrix damage are responsible for the failure of the composite with $\rho = 10$. Furthermore, due to the introduction of Eq. (33), matrix damage is accelerated as interface damage reaches the critical state at the average strain level 6% in the computation of the anisotropic damage model.

The proposed damage model is applied to composites with the two different aspect ratios. The computational results are validated by the micromechanical analysis and experimental data. It is shown that the main damage mechanisms under tension loading are well predicted by the proposed anisotropic damage model.

5.3. *Comparison to micro-pillar experiments in multiple directions*

The anisotropic microstructure of dental enamel indicates a dependence of the material strength on the fiber orientation or loading direction. It is crucial that a successful constitutive model incorporating damage is able to predict this dependence. Therefore, the anisotropic damage model is compared to the micro-pillar tests of Yilmaz et al. (2015) including multiple fiber orientations. According to Bechtle et al. (2012), it is experimentally found that the composite in the first hierarchical level of dental enamel has a very high aspect ratio. The computational investigation suggests that the composite with aspect ratio $\rho = 58$ can reproduce the material behavior and damage mechanisms of the realistic bio-composite in the first hierarchical level of dental enamel (Ma et al., 2016). Hence, for the computation we resort to an aspect ratio $\rho = 58$ for representing the bio-composite in the first hierarchical level of dental enamel.

The stress–strain curves under compression with respect to four different fiber orientations are computed by the proposed anisotropic damage model with the material parameters identified for the composite with the aspect ratio $\rho = 58$ (Table 2). In addition, the initial damage resistance of fiber under tension and compression are identical, $Y_{cf}^{com} = Y_{cf}^{ten}$. The four fiber orientations include the angle between mineral fiber and the loading direction $\theta = 0°$, 23°, 65°, 90°, where $\theta = 0°$ represents the fiber orientation parallel to the loading direction, the mineral fiber is aligned perpendicular to loading direction for $\theta = 90°$. The different fiber orientation result in significantly different stress–strain curves under compression, cf. Fig. 14. For $\theta = 0°$ and $\theta = 23°$, a brittle fracture behavior and a small fracture strain is observed. In contrast, for $\theta = 65°$ and $\theta = 90°$ the stress–strain responses exhibit a gradual damage development and a much lower stiffness. These computation results are consistent with the experimental findings of Yilmaz et al. (2015).

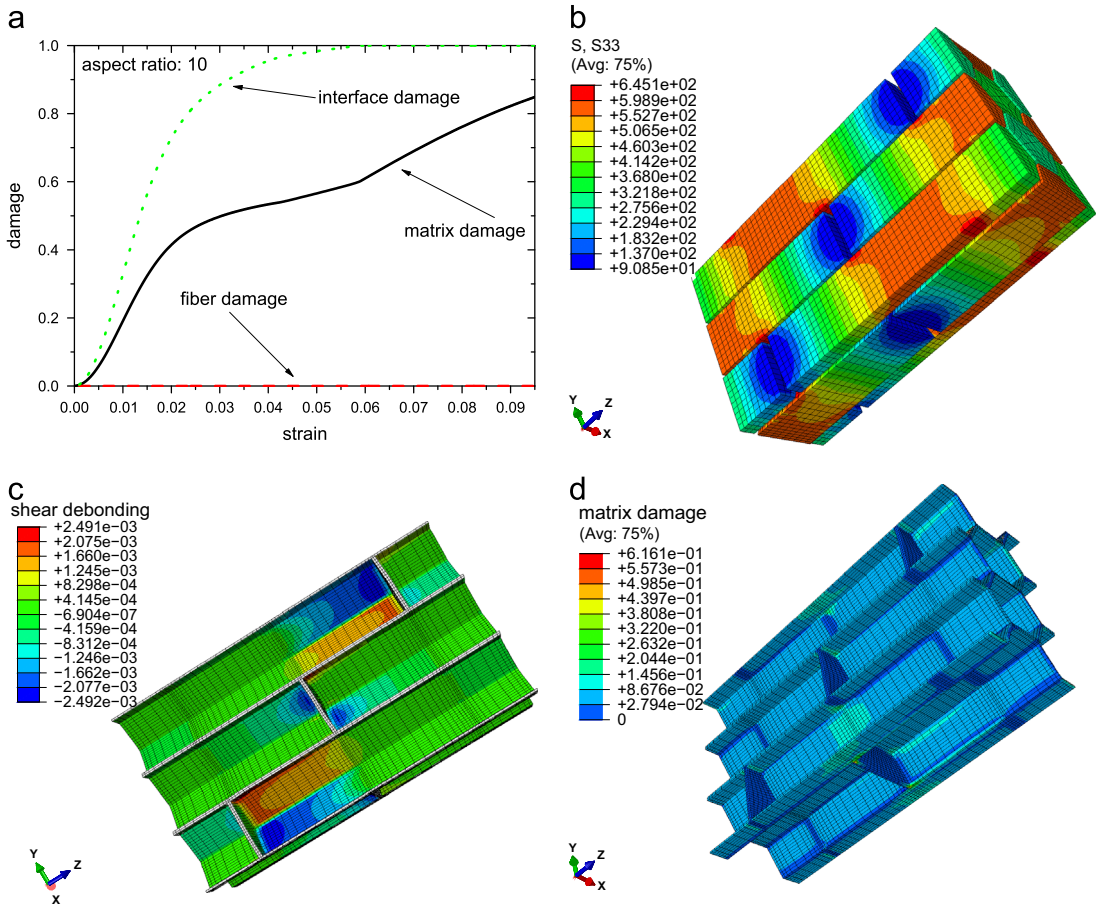

Fig. 13 – Damage evolution process from micromechanical simulation and the anisotropic damage model for the composite with aspect ratio $\rho = 10$. Interface and matrix damage are responsible for failure. The stress level in the fiber is much lower than the strength of fiber.

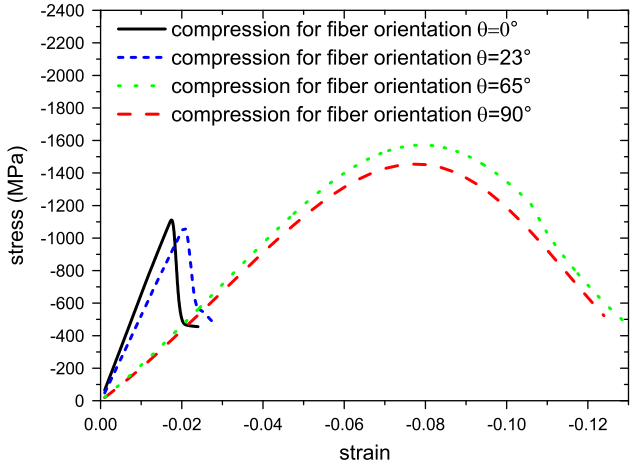

Fig. 14 – stress–strain curves under compression in four different loading directions. The four fiber orientations include the angle between mineral fiber and the loading direction $\theta = 0$ deg, 23 deg, 45 deg, 90 deg.

Moreover, it is noted that fiber damage leads to the final failure for the cases with θ=0° and θ=23° under compression, while some interface and matrix damage exist, but these are not dominant (Fig. 15). For the case of the fiber orientation θ=65°, the protein damage develops rapidly and fiber damage is activated at an average strain level of 11%. Fiber and matrix damage mainly contribute to the failure of the composite. Different to the other cases, only matrix damage is activated for compression perpendicular to fiber direction (θ=90°) leading to collapse of the composite. Regarding the dependence of damage mechanisms on the fiber orientation, the computation prediction is in good agreement with the experimental observation in the micro-pillar experiments by Yilmaz et al. (2015), where protein damage leads to the failure of sample with θ=90° and the fiber damage results in the collapse of the sample with θ=0°.

The predicted strength is compared to the experimentally determined strength in Table 4. The dependence of the compressive failure strength on the fiber orientation is reasonably well captured by the damage model. The highest strength at the first hierarchical level in dental enamel is found in case of the fiber orientation θ=90°, which involve a large deformation (>15%) and gradual development of matrix damage. The failure strength in the cases of θ=0° and θ=23° are nearly identical, where the damage mechanisms occurring in the simulation are similar. The compressive strength is overpredicted for all loading cases compared to the experimental results. It probably results from the

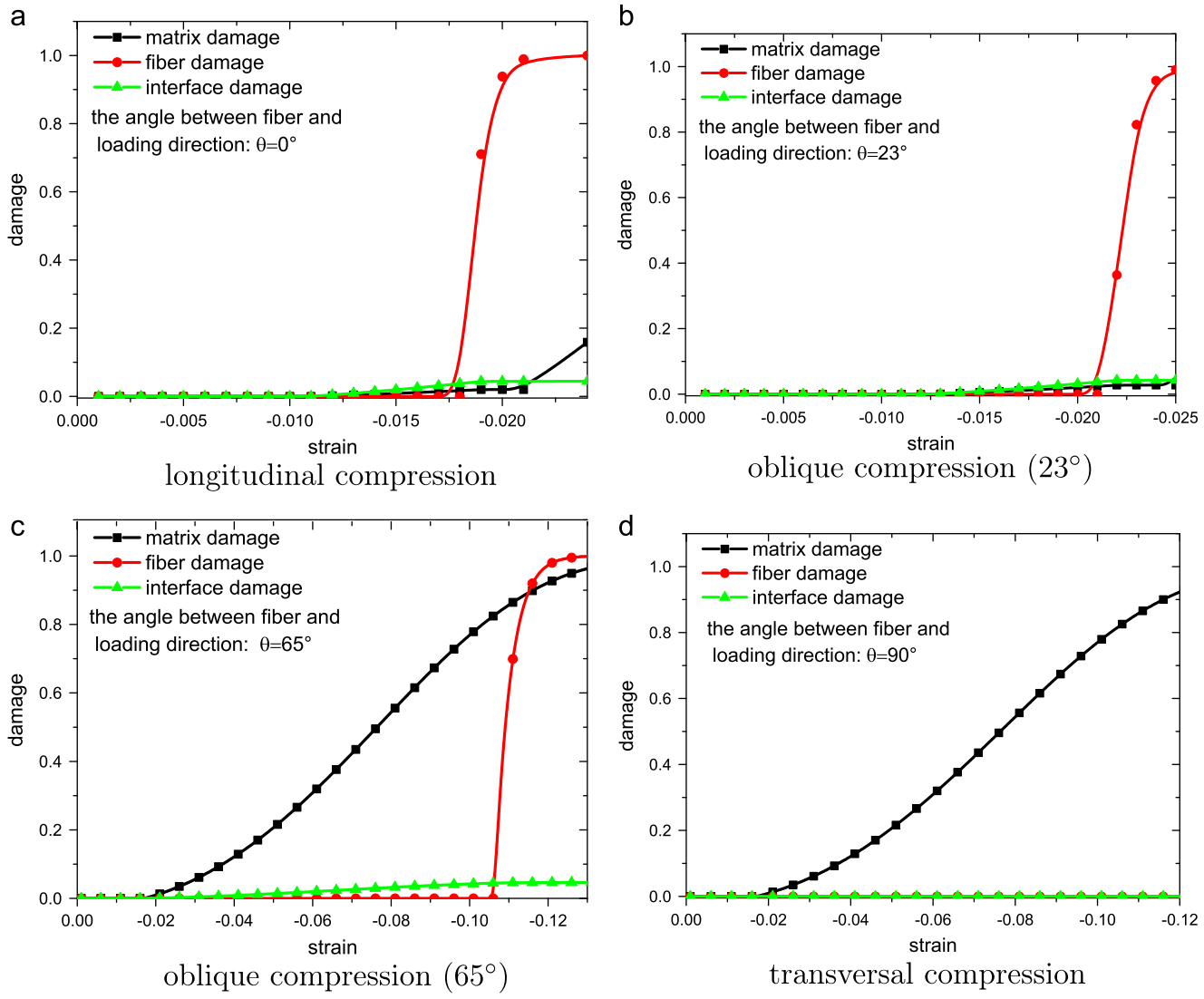

Fig. 15 – Damage evolution curves under compression in different loading directions. Regarding the dependence of damage mechanisms on the fiber orientation, the computation prediction is in good agreement with the experimental observation in the micro-pillar experiments by Yilmaz et al. (2015).

Table 4 – Comparison of experimental and numerical failure strength.

Loading mode	σ_f from simulations	σ_f from experiments (Yilmaz et al., 2015)
Longitudinal	1101 MPa	790±112 MPa
Transversal	1453 MPa	1362±333 MPa
Oblique (23°)	1058 MPa	848 MPa

idealization of fiber orientation in the simulation that all fibers are aligned unidirectionally in the micro-pillar samples, while the experimental observation reveals that HAP crystallites do not align perfectly parallel to each other and seem rather randomly entangled (Yilmaz et al., 2015). In addition, the statistical distributions of the mechanical and geometrical properties of the fibers are not taken into account in the simulation.

6. Conclusions

The present work focuses on proposing the efficient homogenization approach for describing the deformation and damage behavior of the composite at a hierarchical level. For this purpose, an anisotropic damage model has been developed within the framework of finite deformation to capture the deformation and damage mechanisms of dental enamel. In the present damage model, the effect of fiber–protein interaction is taken into account for describing the deformation behavior of bio-composites under general loading conditions. In addition, the tension–compression asymmetry in the hyperelastic deformation behavior is considered in the formulation of the volumetric part of the strain energy. In addition, three different damage mechanisms, namely matrix, interface and fiber damage, are incorporated in the model. The damage potential of matrix and interface

accounts for the interaction between matrix and interface damage.

The anisotropic hyperelastic model coupled with continuum damage mechanics has been applied to the first hierarchical level of dental enamel. To this end, a numerical homogenization scheme has been applied. Micromechanical simulations of a 3D RVE model of dental enamel have been carried out under different loading conditions for identifying the material parameters of the proposed model, first for the deformation parameters, and then for the damage parameters. Afterwards, the damage model has been validated by comparing the stress–strain curve from micro-cantilever beam tests on dental enamel. Additionally, the predicted strength and damage mechanisms under compression in different directions are validated by micro-pillar experiments of dental enamel in multiple directions.

The simulation results show that the proposed damage model is able to predict the deformation and damage behavior of hard bio-composites with different microstructural features under various loading conditions. The progressive damage accumulation law of matrix, interface and fiber damage is in good accordance with the initiation and development of damage in the micromechanical simulations. Moreover, the activated damage mechanisms in the computation under different loading directions are in good agreement with experimental observations of the micro-pillar experiments on dental enamel performed by Yilmaz et al. (2015). The effect of the microstructure characteristics of dental enamel on the mechanical response is captured by the proposed anisotropic damage model with a proper set of material parameters.

With the presented model, which contains explicit description of fiber, matrix and interface behavior, and a physically based parameter identification procedure, we have developed a sound method, which can be employed for predicting the homogenized constitutive behavior of bio- and bio-inspired fiber-reinforced composites also in large scale simulations without explicitly considering and modeling the microstructure. The present model provides a modeling approach to study, understand the structure–property relationship over different hierarchical levels and the role of the hierarchical level on the damage-tolerance behavior of dental enamel.

Acknowledgments

Partial financial support by the ACE-Centre (Institute of Materials Research, Helmholtz-Zentrum Geesthacht, Germany) is gratefully acknowledged. Partial financial support by the German Research Foundation (DFG) via SFB 986 "M^3" (projects A5, B6) is also gratefully acknowledged.

Appendix A. Nomenclature

A.1. Scalars

A	damage resistance function of matrix and interface
B_1, B_2	parameter for evolution equation of α
C_1, C_2	parameter for Ψ_m^0
C_3, C_4	parameter for Ψ_f^0
C_{int}	fiber–matrix interaction parameter for Ψ_{int}^0
D_{m}	matrix damage
D_{f}	fiber damage
D_{int}	interface damage
I_1, I_2, I_3	invariants of $\boldsymbol{C}$
I_4,I_5	anisotropic invariants of $\boldsymbol{C}$
K	parameter for ψ_m^0
J	det($\boldsymbol{F}$)
T_0	parameter of the cohesive interface: fracture strength
Y	damage driving force
Y_0	initial damage resistance of the matrix
Y_{m}	damage driving force of the matrix
Y_{eq}	equivalent damage driving force
Y_{f}	damage driving force of the fiber
Y_{cf}	parameter for the fiber damage evolution (initial resistance)
Y_{int}	damage driving force of the interface
Z	damage resistance function of the fiber
b_1, b_2	parameter for evolution equation of α
b_3	parameter for evolution equation of D_{f}
p_{m}	partial hydrostatic pressure of the matrix
Γ_0	parameter of the cohesive interface: fracture energy
Ψ	free energy density
Ψ^0	free energy density of undamaged material
Ψ_{m}	free energy density of matrix material
Ψ_{f}	free energy density of fiber
Ψ_{int}	free energy density of interface
α	damage strengthening for matrix and interface
β	tension–compression asymmetry parameter for ψ_m^0
λ_{mi}	damage multiplier for matrix and interface
λ_{f}	damage multiplier for fiber
ϕ	fiber–matrix shear interaction
θ	fiber angle with respect to loading direction

A.2. Vectors and tensors

$\boldsymbol{B}$	left Cauchy–Green deformation tensor
$\boldsymbol{C}$	right Cauchy–Green deformation tensor
$\boldsymbol{F}$	deformation gradient
$\boldsymbol{S}$	second Piola Kirchhoff stress tensor
$\mathbf{a}_0$	fiber direction (reference configuration)
$\mathbf{a}$	fiber direction (current configuration)

Appendix B. Fiber–matrix interaction

As shown in Fig. 2, the fiber orientation vector $\mathbf{a}_0$ coincides with the normal direction $\mathbf{n}_0$ of matrix plane with the differential area element dS_0 in the reference configuration, i.e., $\mathbf{a}_0 = \mathbf{n}_0$. After a deformation $\boldsymbol{F}$, the normal direction $\mathbf{n}$ of the deformed differential area element dS is calculated by using Nanson's relation

$$\mathbf{n}=\frac{1}{}\left|\mathbf{n}_0\cdot\boldsymbol{F}^{-1}\right|\mathbf{n}_0\cdot\boldsymbol{F}^{-1}=\frac{1}{}\left|\mathbf{a}_0\cdot\boldsymbol{F}^{-1}\right|\mathbf{a}_0\cdot\boldsymbol{F}^{-1} \tag{B.1}$$

with the norm of the vector $\left|\mathbf{a}_0\cdot\boldsymbol{F}^{-1}\right| = \sqrt{\mathbf{a}_0\cdot\boldsymbol{F}^{-1}\cdot\boldsymbol{F}^{-\mathrm{T}}\cdot\mathbf{a}_0}=\sqrt{\mathbf{a}_0\cdot\boldsymbol{C}^{-1}\cdot\mathbf{a}_0}$. The deformed fiber direction vector $\mathbf{a}$ is calculated with the deformation gradient tensor $\boldsymbol{F}$ as

$$\mathbf{a}=\frac{1}{\lambda_{\mathrm{F}}}\boldsymbol{F}\cdot\mathbf{a}_0, \tag{B.2}$$

where λ_{F} is the fiber stretch during the deformation.

The fiber–matrix interaction between the matrix and the fiber is measured by the relative angle θ illustrated in Fig. 2

$$\cos\theta=\mathbf{n}\cdot\mathbf{a}=\frac{1}{}\left|\mathbf{n}_0\cdot\boldsymbol{F}^{-1}\right|\frac{1}{\lambda_{\mathrm{F}}}\mathbf{a}_0\cdot\boldsymbol{F}^{-1}\cdot\boldsymbol{F}\cdot\mathbf{a}_0=\sqrt{\frac{1}{\mathbf{a}_0\cdot\boldsymbol{C}^{-1}\cdot\mathbf{a}_0\frac{1}{I_4}}}. \tag{B.3}$$

Following the Cayley–Hamilton theorem, the following characteristic equation of the right Cauchy–Green deformation tensors $\boldsymbol{C}$ should be satisfied,

$$\boldsymbol{C}^3-I_1\boldsymbol{C}^2+I_2\boldsymbol{C}-I_3\boldsymbol{I}=0, \tag{B.4}$$

where $\boldsymbol{I}$ is the second order identity tensor. By multiplying Eq. (B.4) with $\boldsymbol{C}^{-1}$, one has

$$\boldsymbol{C}^{-1}=\frac{1}{I_3}\left[\boldsymbol{C}^2-I_1\boldsymbol{C}+I_2\boldsymbol{I}\right] \tag{B.5}$$

Substituting this expression into Eq. (B.3), we obtain

$$\cos\theta=\mathbf{n}\cdot\mathbf{a}=\sqrt{\frac{I_3}{[I_5-I_1I_4+I_2]I_4}}. \tag{B.6}$$

Appendix C. Stress tensor derivation based on the hyperelastic energy coupled with damage

According to Eq. (5), the second Piola–Kirchhoff stress tensor is obtained via

$$\begin{aligned}\boldsymbol{S}=2\frac{\partial\Psi}{\partial\boldsymbol{C}}=&2[1-D_{\mathrm{m}}]\left\{\frac{\partial\Psi_{\mathrm{m}}^0}{\partial J}\frac{\partial J}{\partial\boldsymbol{C}}+\frac{\partial\Psi_{\mathrm{m}}^0}{\partial\bar{I}_1}\frac{\partial\bar{I}_1}{\partial\boldsymbol{C}}\right\}+2[1-D_{\mathrm{f}}][1-D_{\mathrm{int}}]\frac{\partial\Psi_{\mathrm{f}}^0}{\partial I_4}\frac{\partial I_4}{\partial\boldsymbol{C}}\\&+2[1-D_{\mathrm{int}}]\left\{\frac{\partial\Psi_{\mathrm{int}}^0}{\partial I_1}\frac{\partial I_1}{\partial\boldsymbol{C}}+\frac{\partial\Psi_{\mathrm{int}}^0}{\partial I_2}\frac{\partial I_2}{\partial\boldsymbol{C}}+\frac{\partial\Psi_{\mathrm{int}}^0}{\partial I_3}\frac{\partial I_3}{\partial\boldsymbol{C}}+\frac{\partial\Psi_{\mathrm{int}}^0}{\partial I_4}\frac{\partial I_4}{\partial\boldsymbol{C}}+\frac{\partial\Psi_{\mathrm{int}}^0}{\partial I_5}\frac{\partial I_5}{\partial\boldsymbol{C}}\right\}.\end{aligned} \tag{C.1}$$

The derivatives of the strain invariant with respect to the right Cauchy–Green tensor are derived as follows:

$$\begin{aligned}&\frac{\partial J}{\partial\boldsymbol{C}}=\frac{J}{2}\boldsymbol{C}^{-1};\quad\frac{\partial\bar{I}_1}{\partial\boldsymbol{C}}=J^{-2/3}\left[\mathbb{I}-\frac{1}{3}\boldsymbol{C}\otimes\boldsymbol{C}^{-1}\right]:\boldsymbol{I}\\&\frac{\partial I_2}{\partial\boldsymbol{C}}=I_1\boldsymbol{I}-\boldsymbol{C};\quad\frac{\partial I_3}{\partial\boldsymbol{C}}=I_3\boldsymbol{C}^{-1};\\&\frac{\partial I_4}{\partial\boldsymbol{C}}=\mathbf{a}_0\otimes\mathbf{a}_0;\quad\frac{\partial I_5}{\partial\boldsymbol{C}}=\mathbf{a}_0\otimes\boldsymbol{C}\cdot\mathbf{a}_0+\mathbf{a}_0\cdot\boldsymbol{C}\otimes\mathbf{a}_0\end{aligned} \tag{C.2}$$

where $\mathbb{I}=\delta_{\mathrm{ik}}\delta_{\mathrm{jl}}$ is the fourth-order identity tensor and $\boldsymbol{I}=\delta_{\mathrm{ij}}$ is the second-order unit tensor.

With the push-forward operation $\sigma=J^{-1}\boldsymbol{F}\cdot\boldsymbol{S}\cdot\boldsymbol{F}^{\mathrm{T}}$, the Cauchy stress tensor that measures the internal force in the deformed configuration reads

$$\begin{aligned}\boldsymbol{\sigma}=&2J^{-1}[1-D_{\mathrm{m}}]\left\{\frac{\partial\Psi_{\mathrm{m}}^0}{\partial J}\frac{J}{2}\boldsymbol{I}+\frac{\partial\Psi_{\mathrm{m}}^0}{\partial\bar{I}_1}\left[\bar{\boldsymbol{B}}-\frac{1}{3}\bar{I}_1\boldsymbol{I}\right]\right\}\\&+2J^{-1}[1-D_{\mathrm{f}}][1-D_{\mathrm{int}}]\frac{\partial\Psi_{\mathrm{f}}^0}{\partial I_4}I_4\mathbf{a}\otimes\mathbf{a}\\&+2J^{-1}[1-D_{\mathrm{int}}]\left\{\frac{\partial\Psi_{\mathrm{int}}^0}{\partial I_1}\boldsymbol{B}+\frac{\partial\Psi_{\mathrm{int}}^0}{\partial I_2}\left[I_2\boldsymbol{I}-I_3\boldsymbol{B}^{-1}\right]\right.\\&\left.+\frac{\partial\Psi_{\mathrm{int}}^0}{\partial I_3}I_3\boldsymbol{I}+\frac{\partial\Psi_{\mathrm{int}}^0}{\partial I_4}I_4\mathbf{a}\otimes\mathbf{a}+\frac{\partial\Psi_{\mathrm{int}}^0}{\partial I_5}I_4[\mathbf{a}\otimes\boldsymbol{B}\cdot\mathbf{a}+\mathbf{a}\cdot\boldsymbol{B}\otimes\mathbf{a}]\right\}.\end{aligned} \tag{C.3}$$

Here, the left Cauchy–Green deformation tensors is defined as $\boldsymbol{B}=\boldsymbol{F}\cdot\boldsymbol{F}^{\mathrm{t}}$ and its isochoric part as $\bar{\boldsymbol{B}}=\bar{\boldsymbol{F}}\cdot\bar{\boldsymbol{F}}^{\mathrm{t}}=J^{-2/3}\boldsymbol{B}$ with $\bar{I}_1=\mathrm{tr}\,\bar{\boldsymbol{C}}=\mathrm{tr}\,\bar{\boldsymbol{B}}$.

Appendix D. Hyperelastic model: material parameter identification

Young's modulus and Poission ratio of the protein are given by $E=900$ MPa, $\nu=0.495$, whereas we have $E=80$ GPa, $\nu=0.23$ for the mineral fibers. There are 7 material parameters to be identified in the hyperelastic part of the proposed model: C_1, C_2, C_3, C_4, K, β, C_{int}. They are identified by adjusting the analytical solution for the anisotropic model to the numerical results of the micromechanical model subjected to four loading conditions: deformation κ of shearing in the transverse plane, tension in fiber direction, compression in transverse direction and shearing along the fiber direction.

The material parameters C_1 and C_2 related to the isotropic part of strain energy density are obtained from the simulation results of shear in transverse plane case (shear mode 1, Fig. 4d). For this loading case, the Cauchy shear stress reads

$$\tau=2C_1C_2\exp(C_2\kappa^2)\kappa. \tag{D.1}$$

The parameters K and β in the volumetric part of the free energy are fitted by the simulation under compression in any transverse direction (Fig. 4b and c). The Cauchy stress is calculated by

$$\sigma=\frac{K}{\beta}\left[\frac{1}{\kappa}-\frac{1}{\kappa^{\beta+1}}\right]+\frac{4}{3}C_1C_2\exp\left(C_2\left[\kappa^{4/3}+2\kappa^{-2/3}-3\right]\right)\left[\kappa^{1/3}-\kappa^{-5/3}\right]. \tag{D.2}$$

In the case of tension in fiber direction (Fig. 4a), the fourth strain invariant I_4 is computed by $I_4=\mathbf{a}_0\cdot\boldsymbol{C}\cdot\mathbf{a}_0=\kappa^2$ with the fiber orientation $\mathbf{a}_0=[0,0,1]$. The material parameters C_3 and C_4 in the strain energy density of the fiber can, thus, be obtained from

$$\begin{aligned}\sigma=&\frac{K}{\beta}\left[\frac{1}{\kappa}-\frac{1}{\kappa^{\beta+1}}\right]+\frac{4}{3}C_1C_2\exp\left(C_2\left[\kappa^{4/3}+2\kappa^{-2/3}-3\right]\right)\left[\kappa^{1/3}-\kappa^{-5/3}\right]\\&+2C_3C_4\exp\left(C_4\left[\kappa^2-1\right]^2\right)\kappa\left[\kappa^2-1\right].\end{aligned} \tag{D.3}$$

Finally, the material parameter C_{int} in the strain energy term of the fiber–matrix interaction is obtained by fitting the simulated average stress–strain curve in the micromechanical analysis under shear along fiber direction (shear mode 2, Fig. 4e). The Cauchy stress is computed as

$$\tau=2C_1C_2\exp(C_2\kappa^2)\kappa+4C_{\mathrm{int}}\kappa^3. \tag{D.4}$$

The material parameters of the anisotropic hyperelastic model are listed in Table 1 for three different aspect ratios. We set identical material parameters of the isotropic part of the strain energy density function, C_1, C_2 for composites with different aspect ratios, since the aspect ratio has minimal influence on the isotropic part of strain energy density function.

REFERENCES

An, B., Wang, R., Arola, D., Zhang, D., 2015. Damage mechanisms in uniaxial compression of single enamel rods. J. Mech. Behav. Biomed. Mater. 42, 1–9.

An, B., Wang, R., Zhang, D., 2012. Role of crystal arrangement on the mechanical performance of enamel. Acta Biomater. 8, 3784–3793.

Bar-On, B., Wagner, H.D., 2011. Mechanical model for staggered bio-structure. J. Mech. Phys. Solids 59, 1685–1701.

Bargmann, S., Scheider, I., Xiao, T., Yilmaz, E., Schneider, G.A., Huber, N., 2013. Towards bio-inspired engineering materials: modeling and simulation of the mechanical behavior of hierarchical bovine dental structure. Comput. Mater. Sci. 79, 390–401.

Barthelat, F., 2014. Designing nacre-like materials for simultaneous stiffness, strength and toughness: optimum materials, composition, microstructure and size. J. Mech. Phys. Solids 73, 22–37.

Bechtle, S., Ang, S.F., Schneider, G.A., 2010. On the mechanical properties of hierarchically structured biological materials. Biomaterials 31, 6378–6385.

Bechtle, S., Ozcoban, H., Lilleodden, E.T., Huber, N., Schreyer, A., Swain, M.V., Schneider, G.A., 2012. Hierarchical flexural strength of enamel: transition from brittle to damage-tolerant behavior. J. R. Soc. Interface 9, 1265–1274.

Chaboche, J.L., Lesne, P.M., Maire, J.F., 1995. Continuum damage mechanics, anisotropy and damage deactivation for brittle materials like concrete and ceramic composites. Int. J. Damage Mech. 4, 5–22.

Chen, P.Y., McKittrick, J., Meyers, M.A., 2012. Biological materials: functional adaptations and bioinspired designs. Prog. Mater. Sci. 57, 1492–1704.

Chen, Q., Pugno, N.M., 2013. Bio-mimetic mechanisms of natural hierarchical materials: a review. J. Mech. Behav. Biomed. Mater. 19, 3–33.

Coleman, B.D., Noll, W., 1963. The thermodynamics of elastic materials with heat conduction and viscosity. Arch. Ration. Mech. Anal. 13, 167–178.

deBotton, G., Hariton, I., Socolsky, E.A., 2006. Neo-Hookean fiber-reinforced composites in finite elasticity. J. Mech. Phys. Solids 54, 533–559.

Ehret, A.E., Itskov, M., 2009. Modeling of anisotropic softening phenomena: application to soft biological tissues. Int. J. Plast. 25, 901–919.

Espinosa, H.D., Rim, J.E., Barthelat, F., Buehler, M.J., 2009. Merger of structure and material in nacre and bone – perspectives on de novo biomimetic materials. Prog. Mater. Sci. 54, 1059–1100.

Flory, P.J., 1961. Thermodynamic relations for highly elastic materials. Trans. Faraday Soc. 57, 829–838.

Fratzl, P., Weinkamer, R., 2007. Nature's hierarchical materials. Prog. Mater. Sci. 52, 1263–1334.

Gao, H., Ji, B., Jäger, I.L., Arzt, E., Fratzl, P., 2003. Materials become insensitive to flaws at nanoscale: lessons from nature. Proc. Natl. Acad. Sci. U. S. A. 100, 5597–5600.

Gasser, T.C., Ogden, R.W., Holzapfel, G.A., 2006. Hyperelastic modeling of arterial layers with distributed collagen fibre orientations. J. R. Soc. Interface 3, 15–35.

Guo, Z., Shi, X., Chen, Y., Chen, H., Peng, X., Harrison, Philip., 2014. Mechanical modeling of incompressible particle-reinforced Neo-Hookean composites based on numerical homogenization. Mech. Mater. 70, 1–17.

Holzapfel, G.A., Gasser, T.C., Ogden, R.W., 2000. A new constitutive framework for arterial wall mechanics and a comparative study of material models. J. Elast. 61, 1–48.

Humburg, H., Volkmann, E., Koch, D., Müssig, J., 2014. Combination of biological mechanisms for a concept study of a fracture-tolerant bio-inspired ceramic composite material. J. Mater. Sci. 49, 8040–8050.

Jäger, I., Fratzl, P., 2000. Mineralized collagen fibrils: a mechanical model with a staggered arrangement of mineral particles. Biophys. J. 79, 1737–1746.

Lapczyk, I., Hurtado, J.A., 2007. Progressive damage modeling in fiber-reinforced materials. Compos. Part A: Appl. Sci. Manuf. 38, 2333–2341.

Lu, C., Nakamura, T., Korach, C.S., 2012. Effective property of tooth enamel: monoclinic behavior. J. Biomech. 45, 1437–1443.

Ma, S., Scheider, I., Bargmann, S., 2016. Continuum damage modeling and simulation of hierarchical dental enamel. Model. Simul. Mater. Sci. Eng. 24, 045014.

Maimí, P., Camanho, P.P., Mayugo, J.A., Dávila, C.G., 2007. A continuum damage model for composite laminates: part I – constitutive model. Mech. Mater. 39, 897–908.

Mengoni, M., Ponthot, J.P., 2015. A generic anisotropic continuum damage model integration scheme adaptable to both ductile damage and biological damage-like situations. Int. J. Plast. 66, 46–70.

Ogden, R.W., 1972. Large deformation isotropic elasticity-on the correlation of theory and experiment for the compressible rubberlike solids. Proc. R. Soc. Lond. A 328, 567–583.

Peña, E., 2011. Prediction of the softening and damage effects with permanent set in fibrous biological materials. J. Mech. Phys. Solids 59, 1808–1822.

Peng, X.Q., Guo, Z.Y., Moran, B., 2006. An anisotropic hyperelastic constitutive model with fiber–matrix shear interaction for the human annulus fibrosus. J. Appl. Mech. 73, 815–824.

Scheider, I., Xiao, T., Yilmaz, E., Schneider, G., Huber, N., Bargmann, S., 2015. Damage modeling of small scale experiments on dental enamel with hierarchical microstructure. Acta Biomater. 15, 244–253.

Vasiukov, D., Panier, S., Hachemi, A., 2015. Non-linear material modeling of fiber-reinforced polymers based on coupled viscoelasticity–viscoplasticity with anisotropic continuous damage mechanics. Compos. Struct. 132, 527–535.

Yeoh, O.H., 1993. Some forms of strain energy function for rubber. Rubber Chem. Technol. 66, 754–771.

Yilmaz, E.D., Schneider, G.A., Swain, M.V., 2015. Influence of structural hierarchy on the fracture behavior of tooth enamel. Philos. Trans. R. Soc. Lond. A: Math. Phys. Eng. Sci. 373, 20140130.

Yilmaz, E.D., Jelitto, H., Schneider, G.A., 2015. Uniaxial compressive behavior of micro-pillars of dental enamel characterized in multiple directions. Acta Biomater. 16, 187–195.